

© Copyright 2017

Shane Colburn

Dielectric Metasurface Optics: A New Platform for Compact Optical Sensing

Shane Colburn

A thesis

submitted in partial fulfillment of the
requirements for the degree of

Master of Science in Electrical Engineering

University of Washington

2017

Committee:

Arka Majumdar

Lih Y. Lin

Program Authorized to Offer Degree:

Electrical Engineering

University of Washington

Abstract

Dielectric Metasurface Optics: A New Platform for Compact Optical Sensing

Shane Colburn

Chair of the Supervisory Committee:
Assistant Professor Arka Majumdar
Electrical Engineering, Physics

Metasurfaces, the 2D analogue of bulk metamaterials, show incredible promise for achieving nanoscale optical components that could support the growing infrastructure for the Internet of Things (IoT) and future sensing technologies. Consisting of quasiperiodic arrays of subwavelength scattering elements, metasurfaces apply spatial transfer functions to incident wavefronts, abruptly altering properties of light over a wavelength-scale thickness. By appropriately patterning scatterers on the structure, arbitrary functions can be implemented up to the limitations on the scattering properties of the particular elements. This thesis details theoretical work and simulations on the design of scattering elements with advanced capabilities for dielectric metasurfaces, showing polarization-multiplexed operation in the visible regime, multiwavelength capability in the visible regime along with a general methodology for

eliminating chromatic aberrations at discrete wavelengths, and compact and tunable elements for 1550 nm operation inspired by an asymmetric Fabry-Perot cavity. These advancements enhance the capabilities of metasurfaces in the visible regime and help move toward the goal of achieving reconfigurable metasurfaces for compact and efficient optical sensors.

Acknowledgements

This past year I have had amazing opportunities to explore research challenges that I am interested in and advance the state of the art in metasurface optics. The work I completed this past year would not have been possible without the support of my colleagues, friends, and family.

First I want to thank Prof. Arka Majumdar for providing me the opportunity to work on this project. I have learned a lot from him this past year and his mentorship and passion for research have helped guide me along the way. I also want to thank Prof. Scott Hauck for helping to connect me with research with Prof. Arka Majumdar in the first place.

I also would like to thank Alan Zhan for useful discussions and advice regarding metasurface design and operation.

I am very appreciative of the support of my family during this past year and want to thank them for all the encouragement and support they provided that helped to get me to this point. I reserve a very special thanks for Linda Yang for accompanying me this past year and helping me through the demands and hard times of graduate school. Her support has enabled the outcomes of this past year and have made it a wonderful learning experience.

Table of Contents

ACKNOWLEDGEMENTS	5
CHAPTER 1: INTRODUCTION	1
CHAPTER 2: BACKGROUND	3
2.1 METASURFACE OVERVIEW	3
2.2 METASURFACE DESIGN PROCESS.....	4
2.3 STATE-OF-THE-ART METASURFACES	6
2.4 LIMITATIONS	8
2.5 TOWARD COMPACT SENSING AND COMPUTING WITH METASURFACES	9
CHAPTER 3: POLARIZATION-MULTIPLEXED VISIBLE REGIME METASURFACES	11
3.1 SUBWAVELENGTH ELEMENT DESIGN	11
3.2 SIMULATION TESTING RESULTS	14
3.2.1 <i>Hologram</i>	14
3.2.2 <i>Focal Splitting</i>	18
CHAPTER 4: MULTIWAVELENGTH OPERATION.....	21
4.1 DISPERSIVE PHASE ENGINEERING	21
4.2 POLARIZATION CODING	22
4.3 EXPLOITING PHASE SHIFTS GREATER THAN 2π	25
4.3.1 <i>Chromatic Aberrations in Metasurfaces</i>	25
4.3.2 <i>Least Common Multiple Phase Approach</i>	28
CHAPTER 5: TUNABLE ASYMMETRIC ELEMENTS FOR RECONFIGURABLE METASURFACES	32
5.1 ASYMMETRIC FABRY-PEROT TUNABLE PHASE CONCEPT.....	33
5.1.1 <i>Ideal Model</i>	33
5.1.2 <i>Simulated Full Cavity</i>	35
5.2 SINGLE ELEMENT ASYMMETRIC PHASE SHIFTERS	37
5.3 SIMULATION TESTING RESULTS	40
5.3.1 <i>1D Phase Profile Device</i>	41
5.3.2 <i>2D Phase Profile Device</i>	43
CHAPTER 6: CONCLUSION AND OUTLOOK	44
REFERENCES.....	46

Chapter 1: Introduction

Electronic sensors have undergone substantial size reductions over the past few decades, primarily driven by the downscaling of CMOS transistors and improvements in nanofabrication technology. For cameras and image sensors in particular, similar size reductions have occurred as we have seen cameras go from bulky and expensive pieces of equipment to ubiquitous technologies embedded in phones, tablets, etc. In today's optical systems the electronics do not pose much of a fundamental size constraint, but rather the optics themselves are the biggest hindrance to further size reductions. With shorter focal lengths, the bulky glass optics require higher curvatures and occupy greater volumes. As we look toward the near future and observe the explosion in demand for sensors and networks to support the infrastructure of the Internet of Things (IoT), the size constraints of our current optical systems will limit the capabilities of sensors.

To address this challenge, metasurface optics is a promising candidate, enabling nanoscale implementations of conventional optical components using the existing infrastructure for semiconductor fabrication. A variety of metasurface-based implementations of conventional components have already been achieved, but there are still limitations to the metasurface-based approach that hinder the widespread adoption of this methodology.

In this thesis, efforts toward overcoming some of the challenges in metasurface optics are presented. In Chapter 2, background is provided on metasurface operation, design, applications, and limitations. Details on what properties are necessary for a compact optical sensor are also detailed. Chapter 3 examines work toward designing polarization-multiplexed metasurfaces that operate at visible wavelengths. Chapter 4 describes three different approaches that were explored for eliminating chromatic aberrations in metasurfaces, focusing primarily on visible regime

operation. Chapter 5 focuses on the design of tunable dielectric elements which could allow for reconfigurable metasurfaces. Chapter 6 summarizes the work completed in this thesis and concludes.

Chapter 2: Background

2.1 Metasurface Overview

Traditional optical components guide light by refractive, diffractive, and reflective principles. These devices operate by altering the properties of an incident wavefront (e.g. phase, amplitude, and polarization) via propagation within the component's material. Alternatively, some operate by generating interference patterns that give rise to Huygens-Fresnel sources that generate particular field distributions in the far-field. Differences in component geometry and material properties produce propagation characteristics that determine a component's behavior. In metamaterials, volumetric modulation of refractive index on a subwavelength scale allows for unprecedented control of light propagation, enabling novel functionality such as negative refraction^{1,2,3}.

While metamaterial-based optical devices render unique functionality, they are limited by their dependence upon light having to propagate through a bulk medium. Signal loss in the bulk medium is a serious constraint on efficiency and from a practical standpoint, the resolution of 3D fabrication techniques restricts the range of feasible devices^{4,5}. Due to these limitations, the 2D analogue of bulk metamaterials, metasurfaces, have garnered substantial interest in recent years. Rather than modulating refractive index over a volume, metasurfaces are ultra-thin structures patterned at the subwavelength scale with quasi-periodic configurations of scattering elements. By appropriately designing and patterning the scattering elements, metasurfaces implement spatial transfer functions which modify input wavefronts over a wavelength-scale distance. The designed transfer functions spatially modulate the phase and or amplitude⁶. This technique has

enabled ultra-thin metasurface-based lenses, axicons, vortex beam generators, holograms, and other optical devices^{7,8,9,10,11}.

2.2 Metasurface Design Process

While the scattering characteristics of an individual subwavelength element is better described via electromagnetics or effective medium theory, the ensemble operation of all the elements and their spatial transfer function can be understood by Fourier optics. While both phase and amplitude modulation can be used in metasurface design in general, the metasurfaces discussed in this thesis only use phase modulation.

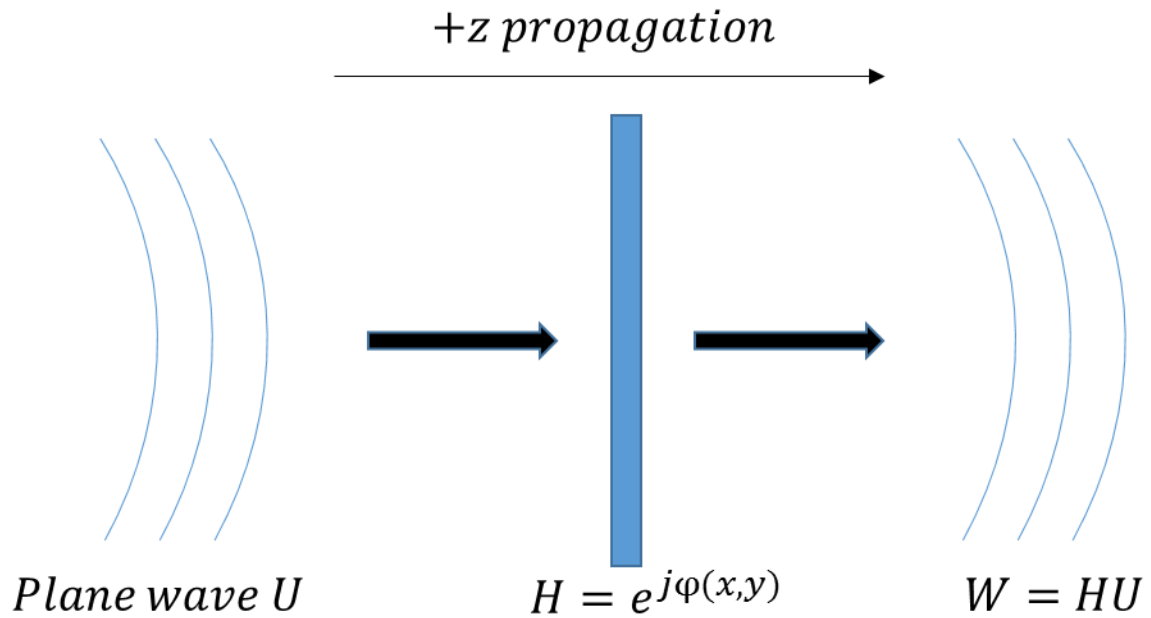


Figure 1: Schematic representation depicting the operation of a metasurface. An incident plane wave U is acted upon by the spatial transfer function of the metasurface to produce an output wave W .

Assume a plane wave $U = Ae^{-j(k_x x + k_y y + k_z z)}$ is incident upon a phase mask in the $z = 0$ plane characterized by a transfer function $H = e^{j\phi(x,y)}$, as in **Figure 1**. This setup presents a model of a metasurface with unit magnitude and a phase distribution $\phi(x, y)$. If the phase

distribution is expressed as a Taylor expansion about the point $r_0 = (x_0, y_0)$, then to first order it can be written as below:

$$(1) \quad \Phi(x, y) \approx \Phi(x_0, y_0) + (x - x_0) \left. \frac{\partial \Phi}{\partial x} \right|_{r=r_0} + (y - y_0) \left. \frac{\partial \Phi}{\partial y} \right|_{r=r_0}$$

If the transfer function H is then applied to the plane wave U , the coefficients of the linear terms in the expansion sum with the x and y wavevector components of the incident wave, giving the result below where all the constant phase terms are bundled into θ :

$$(2) \quad W = HU \approx Ae^{-j \left[\left(\left. \frac{\partial \Phi}{\partial x} \right|_{r=r_0} + k_x \right) x + \left(\left. \frac{\partial \Phi}{\partial y} \right|_{r=r_0} + k_y \right) y + k_z z + \theta \right]}$$

From (2) we see that the gradient of the phase distribution has the effect of changing the wavevector of the incident wave¹². This change in wavevector resulting from the spatial phase function of a mask provides the underlying intuition for how metasurfaces can abruptly alter wavefronts. To achieve a particular optical transformation, the designer first should know how the incident wavevector must change, then using this information the necessary spatial phase function can be derived.

Determining the necessary spatial phase function is the first step in the metasurface design process. This step provides a continuous function of position with the ideal transfer characteristics; however, in terms of implementation such a phase profile cannot be fabricated for it would require infinitesimal resolution. In practice, metasurface phase profiles are broken into a grid of finite unit cells forming a spatially discrete function, analogous to signals in discrete time systems with fixed sampling periods. The metasurface must be designed such that the spatial sampling period satisfies the criterion of the Nyquist-Shannon sampling theorem¹³. In each unit cell an appropriate scattering element is placed such that the necessary phase shift at that point is achieved.

In order to physically implement the discrete phase function on the metasurface, scattering elements which can achieve phase shifts from 0 to 2π are necessary to attain arbitrary phase functions. Selecting scattering elements is often a challenge because of design constraints. The first constraint is the requirement that the unit cell's period be subwavelength. This constraint ensures that the metasurface only passes the zero order diffraction mode¹⁴. A second constraint is that the elements patterned across the surface be of the same height, enabling fabrication of the metasurface with a single lithography stage. With the height of the scattering structures being uniform, a designer is left with a few means by which the phase can be tuned. By changing either the geometry or orientation of the scattering structures, phase shifts spanning 0 to 2π with uniform magnitude can typically be achieved. For example, many metasurfaces utilize Pancharatnam-Berry (PB) phase elements with phase shifts that are proportional to the element's orientation angle within its cell^{7,15,16}. Other phase tuning methods involve adjusting the widths, diameters, or periodicity of the scattering elements^{17,18}.

2.3 State-of-the-art metasurfaces

Metasurfaces have undergone several substantial developments in the past few years. Many of the initial metasurface-based optics used surface plasmon-based scattering elements, requiring the metasurface to be made of metal^{19,20,21,22,23,24}. With metals being so lossy in the optical regime, such structures were confined to operating in reflection mode^{25,26}. Silicon-based metasurfaces helped to overcome this challenge, allowing for metasurfaces that can operate with high efficiency in both reflection and transmission modes in the near-infrared^{7,11,17}. Even more recent developments have shown efficient operation in the visible regime by using lower index materials^{27,28}.

A wide variety of standard optical components have been replicated and successfully tested using metasurface-based implementations. Many of these replicated standard optical components have been downsized substantially in their metasurface-based implementations. More advanced functionalities have also been achieved. Polarization-multiplexed structures have been implemented, allowing for different optical transformations to be achieved depending on the input polarization state; however, these devices have mainly been confined to operating at infrared wavelengths¹¹.

In addition to replicating functionality of conventional refractive and diffractive optics, metasurfaces also enable new functionalities. Recently, in simulation a metasurface combined with graded-index waveguides performed spatial differentiation, integration, and convolution operations on input wavefronts²⁹. In practice it is difficult to achieve such a structure, but a poor man's integrator metasurface was implemented using a reflective plasmonic metasurface³⁰. Metasurfaces have also achieved skin cloaking-like behavior, modifying reflected wavefronts from arbitrarily shaped objects to make them appear as if they are coming off a flat mirror; however, the conventional quasi-conformal mapping technique wherein light is bent around an object has not been achieved³¹. Metasurfaces have also demonstrated capability for observing interesting physical phenomena, such as spin-orbit coupling and the photonic spin hall effect³². While most metasurfaces designed thus far have been static structures with a single functionality, some groups have started developing reconfigurable devices with the ability to tune local phase shifting properties to implement different phase profiles³³. Many of these structures have been limited in terms of efficiency and reconfigurable metasurfaces remains an active research area.

2.4 Limitations

While metasurfaces provide an impressive set of capabilities, there are still substantial limitations to these devices which remain open research challenges. While some groups have demonstrated operation in the visible regime, most devices have been confined to operation in the infrared. Most of the work has been confined to operation in the infrared because the materials used are generally too lossy, having high band gaps or are opaque at visible wavelengths. Without the capability of operating at visible wavelengths, the span of applications for which metasurfaces can work is significantly limited. Additionally, these structures face a variety of aberrations, most prominently perhaps chromatic aberrations. As with any structure which operates based on diffractive principles, the operation of metasurface-based devices deviates substantially from their designed operation as the wavelength changes. There have been attempts at achieving achromatic metasurfaces, but these approaches have only supported multiwavelength operation rather providing a truly broadband achromatic device^{34,35}.

In addition to the aberrations and material constraints of metasurfaces which limit visible regime operation, one of the big open problems in metasurface research is devising a method to achieve phase elements which can be dynamically altered to achieve reconfigurable phase profiles. Achieving this capability would enable the optical equivalent of a field-programmable gate array (FPGA), so that arbitrary optical transformations could be implemented and reprogrammed as desired. To achieve reconfigurable metasurfaces, most approaches consist of locally tuning the refractive index of the phase shifting elements. Unfortunately, changing the refractive index to achieve arbitrary 0 to 2π phase shifts is challenging. The range over which refractive index can be modulated is generally very small, and the nanoscale size constraints of metasurfaces limit the propagation distance and change in phase accumulation that could arise

from a refractive index change. There are some methods by which the refractive index can be changed substantially, as in the case of phase-change materials such as germanium-antimony-tellurium (GST) which was recently used to make a metasurface³³; however, phase change materials can exhibit substantial loss depending on the operating wavelength. A robust and reconfigurable metasurface platform will require phase elements that can be easily tuned without substantial loss in performance.

2.5 Toward Compact Sensing and Computing with Metasurfaces

Image sensors and optical systems in general have undergone dramatic size reductions in the last few decades. Much of this miniaturization has been driven by the advent of compact CMOS sensors. Even smaller imaging systems are desirable though, as nanoscale-imaging systems could revolutionize implantable biosensors and the Internet of Things (IoT). However, systems today are not size-limited by their sensors, rather the size constraint is primarily imposed by the optical elements themselves as short focal length refractive optics require high curvature structures. A methodology for achieving a compact optical sensor would revolutionize optical systems and enable a variety of new technologies.

Metasurface optics provides a unique platform for achieving such sensors, allowing for nanoscale implementations of conventional optics, as well as enabling a whole span of new and interesting optical transformations and capabilities. However, due to some of the current limitations of these devices (e.g. aberrations, limited visible regime operation, limited refractive index modulation range) they are not at the point of development at which such sensors can be implemented.

This thesis details efforts on extending the capabilities of current metasurfaces to overcome some of the existing limitations so that a compact optical sensor may be achieved. In

particular, three distinct focus areas are explored which help to expand the current state of the art devices in metasurface optics. Firstly, polarization-multiplexed metasurfaces are designed and tested in the visible regime. A metasurface platform with polarization-multiplexing capability in the visible regime would enable optical switching capabilities and allow a single optic to perform multiple transformations in parallel. The second focus of this thesis details work towards achieving multiwavelength operation in the visible regime, such that metasurfaces can operate at multiple wavelengths without chromatic aberrations. Such a device could enable nanoscale display technologies if designed for operation at red, green, and blue wavelengths. Additionally, imaging applications could benefit from visible regime optics without chromatic aberrations. Finally, a design is presented for a subwavelength phase shifter which is highly tunable, enabling large changes in phase with minimal change in refractive index. Such a compact phase shifter could enable highly tunable metasurfaces which could be reprogrammed dynamically to implement arbitrary phase profiles. Altogether, the three focus areas detailed in this thesis help to provide incremental development toward the eventual realization of a compact optical sensor.

Chapter 3: Polarization-multiplexed Visible Regime Metasurfaces

Metasurfaces with polarization-multiplexing capabilities have yet to be developed for visible wavelengths. Infrared regime metasurfaces based on elliptical silicon nanoposts were used to generate different patterns depending on the input polarization¹¹. Similarly, reflective plasmonic structures have been used to generate different holograms depending on the input helicity³⁶. These capabilities enable a wide variety of technologies and capabilities for optical systems and sensors. Here the viability of this multiplexing capability is explored for visible regime metasurfaces at 633 nm based on silicon nitride scattering elements. A preliminary set of parameters that provide this capability are found and then tested via FDTD simulations.

3.1 Subwavelength Element Design

The first stage in developing a polarization-multiplexing metasurface required finding subwavelength elements that provide arbitrary and independent 0 to 2π phase shifts for both x and y-polarized input polarizations. This requirement enables each unit cell of the metasurface to produce any desired phase combination (Φ_x, Φ_y) where Φ denotes the phase accumulated on transmission and the subscript denotes the input polarization. Extending this capability of each unit cell to all unit cells of the metasurface then allows for phase functions to be implemented independently for x and y-polarizations.

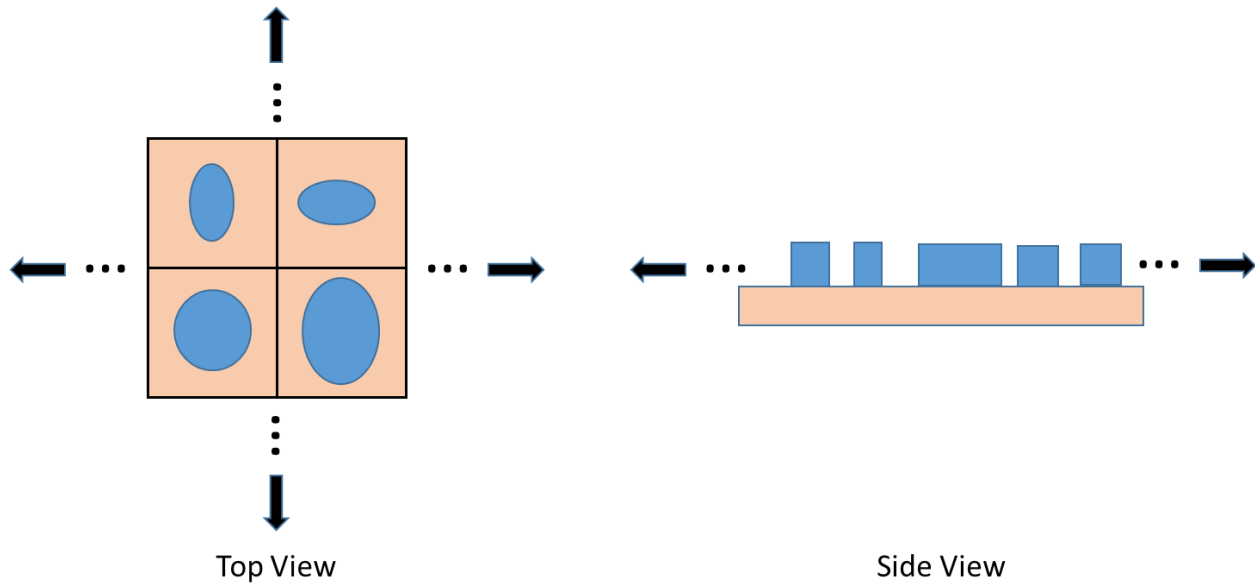


Figure 2: Schematic representation of what the unit cells of the metasurface look like. Each unit cell has a single elliptical post of silicon nitride on top of a silicon dioxide substrate. Both top and side views are shown.

Each unit cell consists of a silicon nitride elliptical post patterned on top of a silicon dioxide substrate. A sample unit cell of the metasurface is depicted in **Figure 2**. By varying the x and y-axis diameters of the ellipse for a fixed thickness and lattice constant, different phase shift combinations for x and y-polarized inputs are achieved. In particular, the rigorous coupled-wave analysis (RCWA) method is used for calculating the transmission coefficients for different parameter combinations. With a post thickness of 700 nm and lattice constant of 500 nm, the transmission coefficients were calculated for x and y-polarizations and are shown in **Figure 3**.

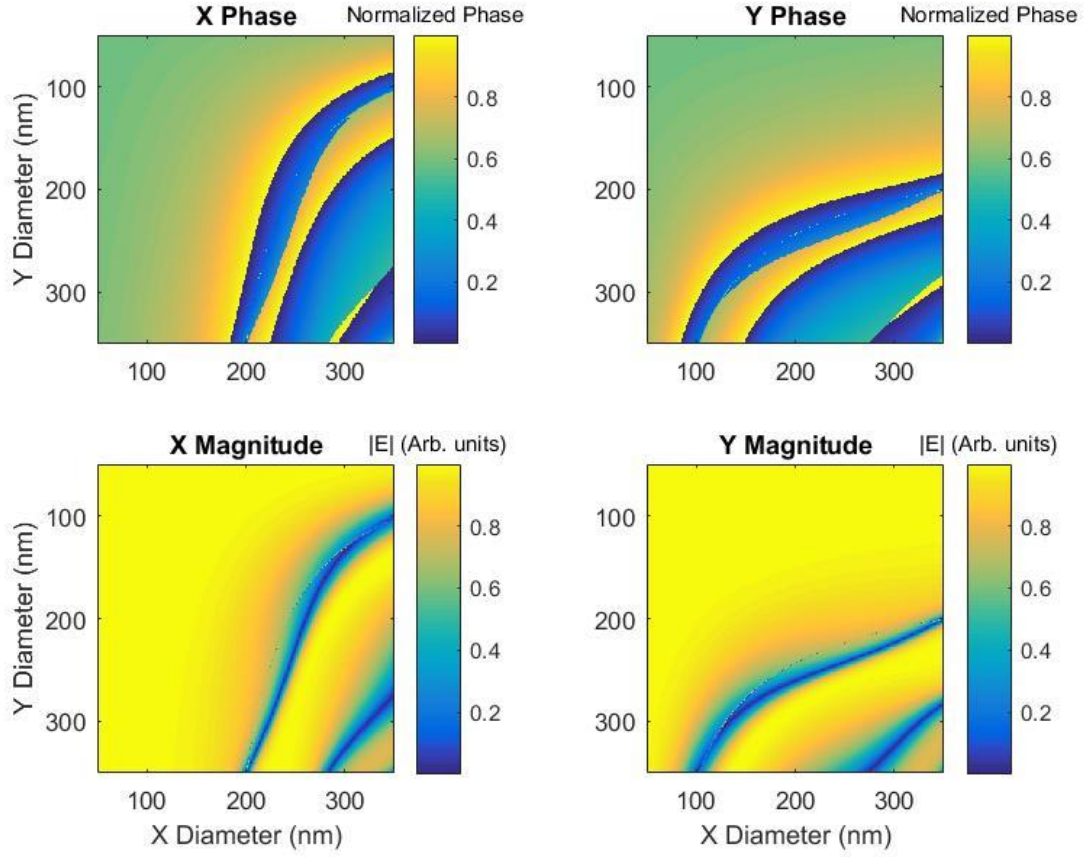


Figure 3: Transmission coefficients for the subwavelength elements that support polarization multiplexing capability. Both the magnitude and phase on transmission are shown for x-polarized and y-polarized inputs.

Upon determining the transmission coefficients for each polarization as a function of the x and y-axis post diameters, this information must be synthesized such that for a desired phase combination (Φ_x, Φ_y) , the corresponding x and y-axis diameters (D_x, D_y) can be determined. This synthesis provides the necessary information to design the scattering elements that would implement the x and y-axis polarization phase profiles. To determine the necessary diameters for a given phase combination, the diameter pair which produces the smallest mean-squared error is selected (i.e. the pair which minimizes the function $E = \frac{1}{2}|t_x - e^{i\Phi_x}|^2 + \frac{1}{2}|t_y - e^{i\Phi_y}|^2$). Using

the data from **Figure 3**, the diameter pairs that minimize the mean-squared error were determined.

3.2 Simulation Testing Results

To assess the parameters determined by the RCWA method, different metasurfaces were designed to demonstrate their multiplexing behavior. Focusing and hologram generation are two of the most basic functionalities achievable by metasurfaces. Two metasurfaces are designed, one which generates different holograms depending on the input polarization, and another which produces a focal spot at a different position depending on the input polarization.

3.2.1 Hologram

To test the multiplexing behavior of the designed subwavelength elements, a metasurface was designed that could produce two different holograms in the far-field depending on the input polarization. In particular, if the input was x-polarized the output would produce an H, whereas if the input was y-polarized the output would produce a V, generating desired far-field magnitude profiles as in **Figure 4**. To do this, the Gerchberg-Saxton (GS) algorithm was used to determine the phase profile necessary to generate each hologram³⁷. The GS algorithm takes as inputs a source magnitude distribution and a desired target plane intensity profile and then iteratively calculates the source phase necessary to produce the given target intensity. The algorithm essentially consists of a sequence of forward and inverse Fourier transforms that with an increasing number of iterations, decreases the error between the Fourier transform of the source field distribution and the desired target intensity. The Fourier transform relationship between the source and the target arises from the fact that the near-field and far-field distributions are in general related by a Fourier transform.

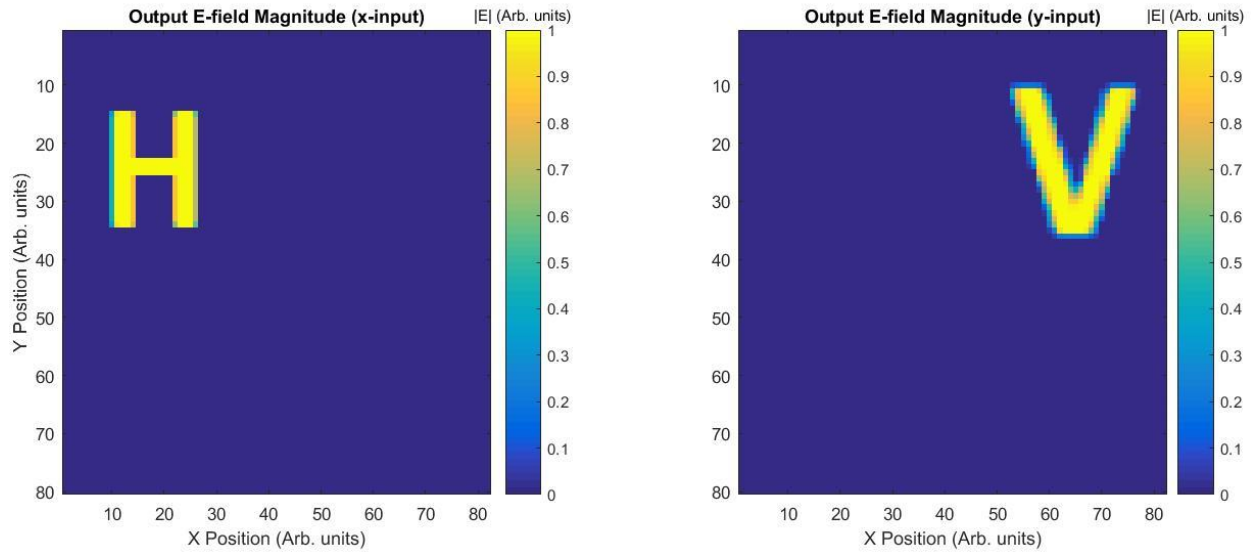


Figure 4: Desired output electric field magnitudes for the designed metasurface. On the left, the magnitude is shown for an x-polarized (horizontal) input. On the right, the magnitude is shown for a y-polarized (vertical) input.

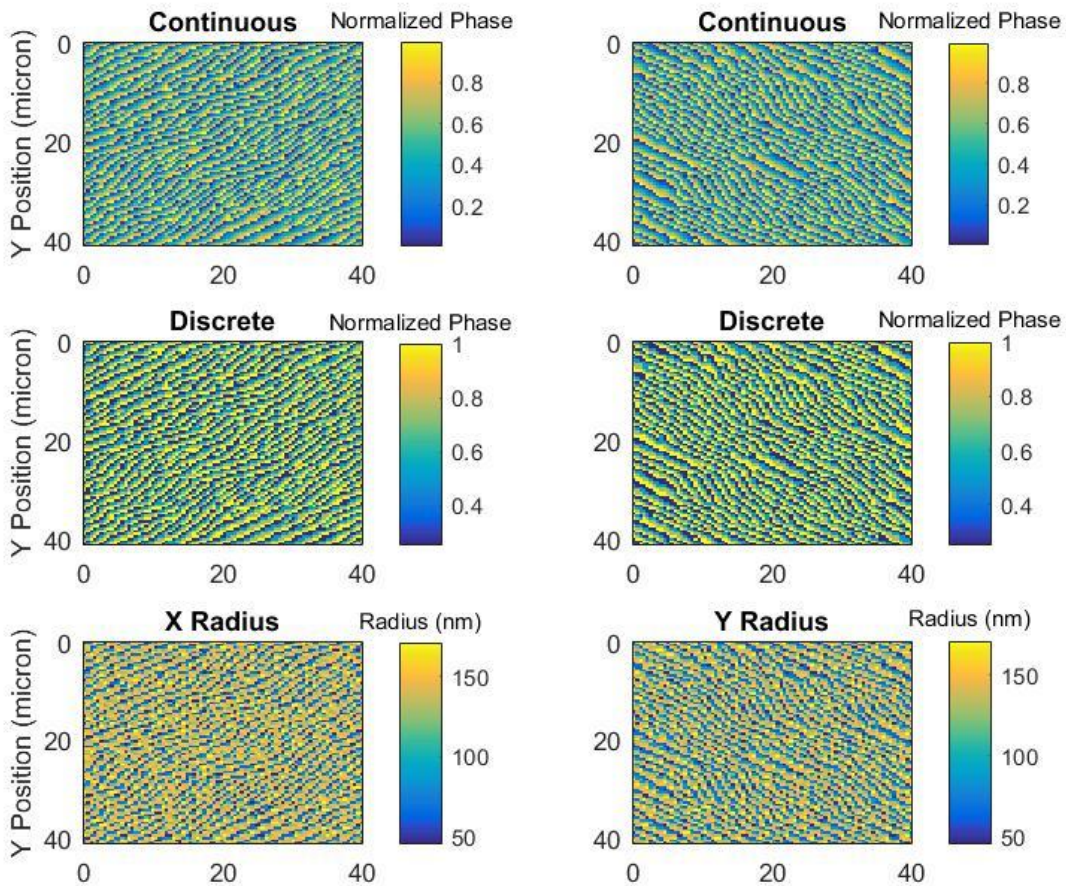


Figure 5: From top to bottom are the continuous phase profiles, discrete phase profiles, and the necessary radii for implementing the desired H and V-shaped hologram patterns in the far-field. The phase profiles for the H-shaped pattern are shown on the left, while those for the V-shaped pattern are shown on the right.

Upon determining the continuous phase functions necessary for both the x and y-polarized target intensities, these phase functions needed to be implemented using the previously designed elliptical nanopost subwavelength elements. Using the designed elements, the post diameters were determined with the minimized mean squared error that provide (Φ_x, Φ_y) pairs in which Φ_x and Φ_y both span 0 to 2π in 4 steps each. In **Figure 5** the continuous and discrete phase functions for the x and y-polarized profiles are depicted along with the necessary x and y-axis ellipse diameters to implement the functions are shown.

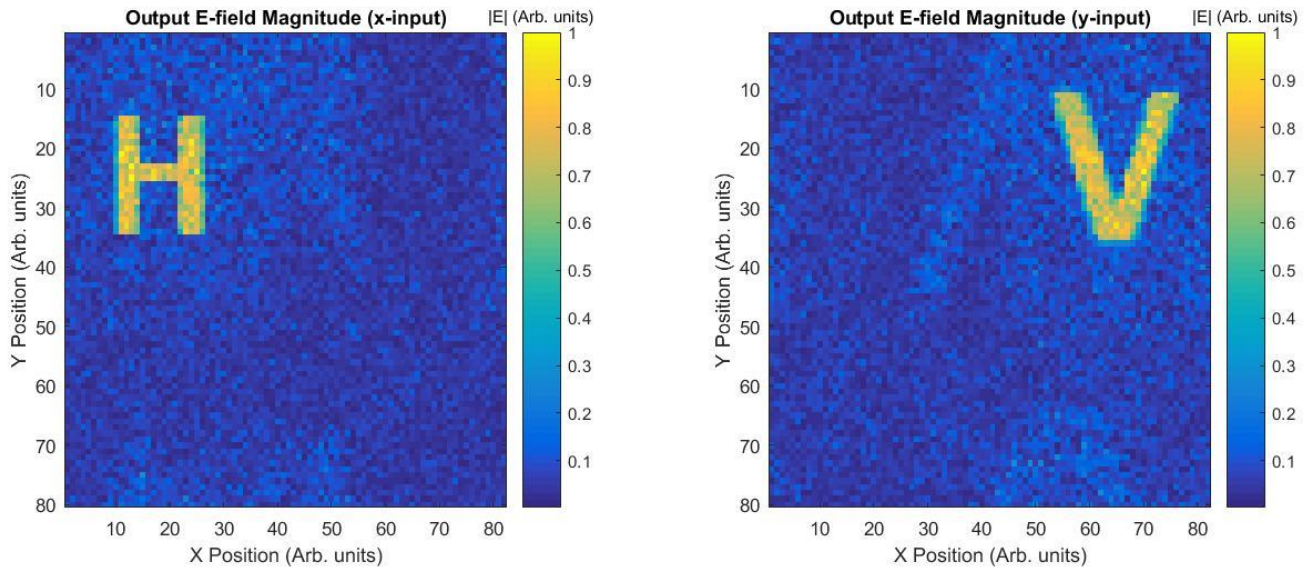


Figure 6: Simulated outputs from the metasurface determined by Fourier transforming the discretized phase profile after being imparted on a unit magnitude incident plane wave. Note that these simulation results assume the metasurface subwavelength elements are perfectly implementing the desired phase at their respective lattice points.

To test the results of the GS algorithm and the phase discretization step, the discrete phase profile was imparted on a source field of unit magnitude and was then Fourier transformed, giving the intensity profile of **Figure 6** which assumes the metasurface subwavelength elements perfectly map to the desired (Φ_x, Φ_y) pair at each unit cell. To assess the subwavelength elements themselves, the metasurface based on the pillar radii in **Figure 3**

was simulated via the finite-difference time-domain (FDTD) method. Due to the computationally expensive nature of this method, the metasurface's output field was only allowed to propagate for a few microns. The FDTD-simulated near-field profile measured a few microns on the output of the metasurface was then Fourier transformed to obtain the far-field characteristics, the results of which are presented in **Figure 7**. It can be seen that from **Figure 4** and **Figure 7** the GS algorithm and the phase discretization step did introduce some error, but the desired holograms are distinct for both polarizations. In going from the ideal discrete profile to the FDTD-simulated metasurface, the desired holograms remained distinct and successfully produced the desired H and V patterns, albeit with some error and a high intensity zero-order diffraction spot which is typical for GS algorithm holograms.

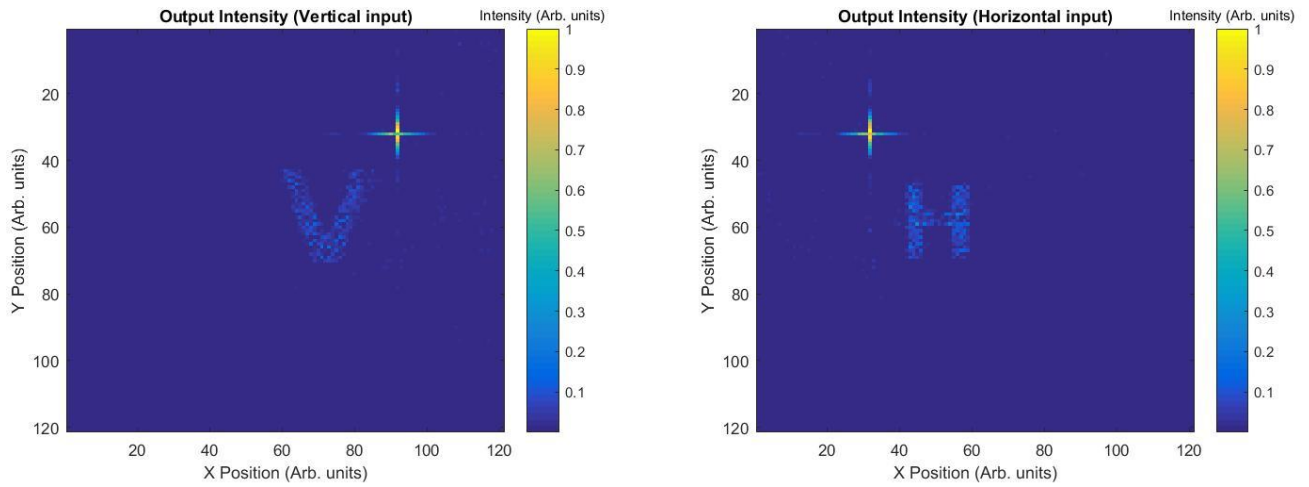


Figure 7: Output intensity profiles for vertical (y-polarized) and horizontal (x-polarized) input conditions. Note that the units are arbitrary as this is in the far-field and that between the two plots the coordinate systems are not equivalent. The high intensity spots correspond to the zero order diffraction spot. The intensity profiles were generated by Fourier transforming the near-field electric field measured above the metasurface via FDTD simulation.

3.2.2 Focal Splitting

Upon successful simulation of the polarization-multiplexed holographic metasurfaces, the designed subwavelength elements needed to be tested further to understand the extent of their capabilities. To do this a metasurface was designed that produces two distinct focal spots for each input polarization. While both spots are located in a parallel plane 15 micron away from the metasurface, for the x-polarized input the spot is located 2 micron to the right of the central axis of the metasurface while for the y-polarized input it is offset 2 micron to the left of the central axis. This metasurface was designed by the same method as for the holographic metasurface except that rather than finding the phase functions for each polarization by the Gerchberg-Saxton algorithm, the phase functions were based on the hyperbolic phase profile necessary for a focusing element. Equation (3) below gives the phase profile for a focusing element with a focal distance of f , an in-plane position coordinate for the focus of (x_0, y_0) , an operating wavelength of λ , and position coordinates in the plane of the metasurface of (x, y) :

$$(3) \Phi(x, y) = \frac{2\pi}{\lambda} (\sqrt{(x - x_0)^2 + (y - y_0)^2 + f^2} - f)$$

The continuous and discrete phase functions are shown in **Figure 8** with the corresponding ellipse diameters which most closely implement the discrete phase function. The metasurface was tested via FDTD simulation and the intensity profiles measured in the designed focal plane are presented in **Figure 9**. The intensity profiles clearly indicate distinct focal spot locations for each input polarization; however, it is also evident that there are some issues with efficiency as light appears to not be fully funneled into the focal spots as there are other bright patches. This is an indication that while the designed subwavelength elements do implement the desired phase functions they have efficiency limitations and are not fully optimized.

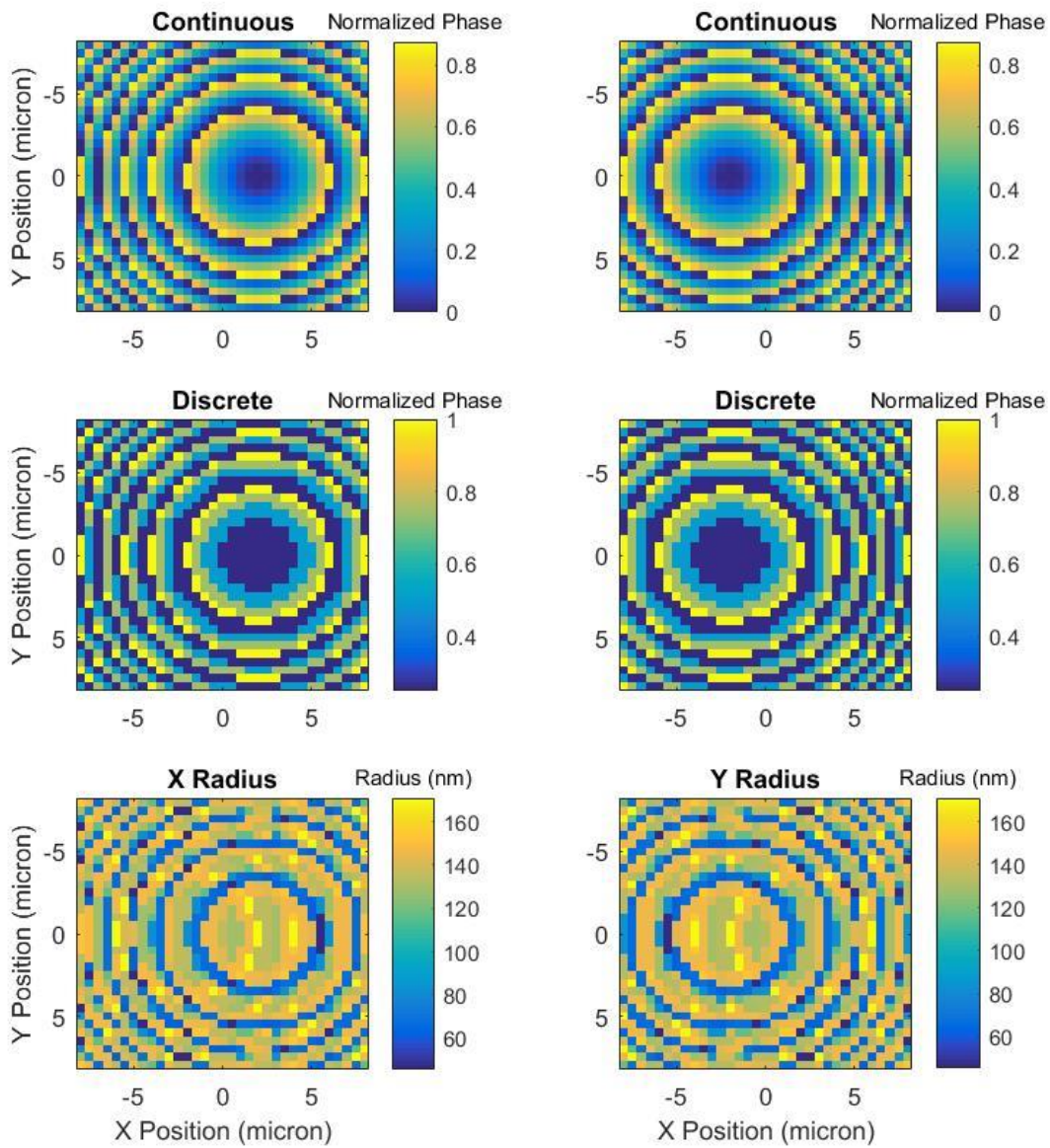


Figure 8: From top to bottom are the continuous phase profiles, discrete phase profiles, and the necessary radii for implementing the focal spots. The phase profiles for the x-polarized input are shown on the left, while those for the y-polarized input are shown on the right.

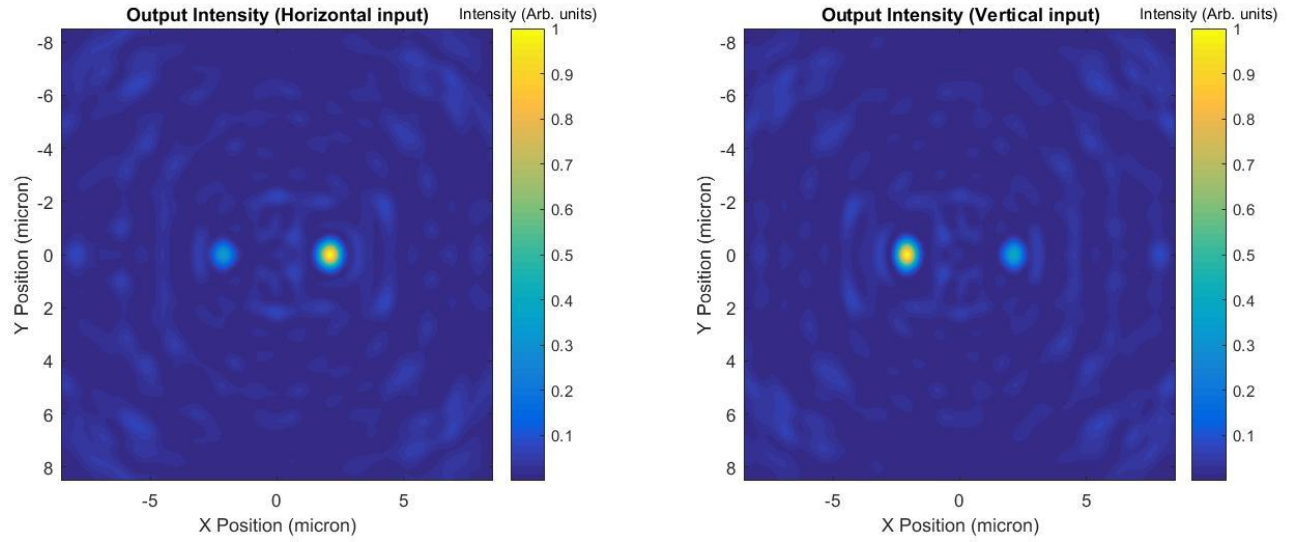


Figure 9: Output intensity profiles for vertical (y -polarized) and horizontal (x -polarized) input conditions via FDTD simulation. The intensity profiles are measured in the designed focal plane parallel to the metasurface. The high intensity spots correspond with the positions of the designed focal spots for each

Chapter 4: Multiwavelength Operation

Chromatic aberrations exist in both refractive and diffractive optics. In refractive optics, the aberrations arise from material dispersion, whereas for diffractive optics the aberrations arise from the spatial arrangement of apertures and structures relative to the wavelength. For conventional refractive optics, achromatic doublet structures and more advanced systems of cascaded components allow for aberration-free operation under particular conditions. These standard aberration-circumventing systems used for refractive devices cannot be easily designed for diffractive optics. In the field of metasurface optics, most devices have been designed to operate at a single wavelength; however, recent work has demonstrated metasurfaces which can operate at multiple discrete wavelengths efficiently.

4.1 Dispersive Phase Engineering

Some groups have demonstrated multiwavelength operation (e.g. lenses with the same focal length for multiple discrete wavelengths) in the infrared by using subwavelength geometries that enable dispersive phase compensation^{34,35}. This technique of dispersive phase compensation is analogous in many respects to the subwavelength element design for polarization-multiplexed metasurfaces—instead of finding a subwavelength element which provides arbitrary phase combination pairs (Φ_x, Φ_y) for two orthogonal polarizations, you find elements which provide arbitrary phase pairs $(\Phi_{\lambda_1}, \Phi_{\lambda_2})$ where λ_1 and λ_2 denote two different input wavelengths. This approach solves the more general problem of making frequency-multiplexed metasurfaces, allowing a single metasurface to perform different optical transformations for different wavelengths. The achromatic problem is just a subset of the wavelength-multiplexing problem in which you design the phase distributions such that each

wavelength produces the same transformation. This approach has been used to demonstrate multiwavelength operation in the infrared.

We explored using this same technique in the visible regime, using wavelengths of 490 nm and 600 nm. Unfortunately, this work did not render any significant results. In simulation, different holograms were generated depending on the input wavelength; however, efficiency was low and there seemed to be crosstalk between the 490 and 600 nm holograms, generating a poor and unintelligible intensity profile. One of the likely issues with this approach, relative to the successful approaches in the infrared, is that the wavelengths considered in this case were much closer, differing by 110 nm, whereas the successful attempts in the infrared differed by at least 300 nm^{34,35}. Having wavelengths that are much closer makes it challenging to achieve differences in phase which allow spanning of all possible $(\Phi_{\lambda_1}, \Phi_{\lambda_2})$ pairs.

4.2 Polarization Coding

To overcome the limitations of the designed metasurfaces for multiplexing at 490 and 600 nm, it was necessary to develop a means by which all possible $(\Phi_{\lambda_1}, \Phi_{\lambda_2})$ pairs could be spanned more easily. Leveraging the previous work with polarization-multiplexing in the visible regime, a new methodology was developed to achieve wavelength multiplexing capability. In particular, the two wavelengths of interest (490 and 600 nm) were encoded with orthogonal polarizations, so that elliptical geometries could be used which exploit the orientation of the incident electric field.

In terms of designing subwavelength elements, the process was similar as for the case of the polarization-multiplexed metasurfaces. With a period of 600 nm and thickness 900 nm, elliptical post x and y-axis diameters were swept from 60 nm to 420 nm and via RCWA the transmission coefficients were calculated for inputs of x-axis polarized 490 nm light and y-axis

polarized 600 nm light. Synthesizing these transmission coefficients under the two different input conditions, the x and y-axis diameter combinations (D_x, D_y) were found which minimize the mean squared error and span all possible $(\Phi_{\lambda_1}, \Phi_{\lambda_2})$ pairs in 4 steps from 0 to 2π each. The transmission coefficients as a function of post diameters are shown in **Figure 10**.

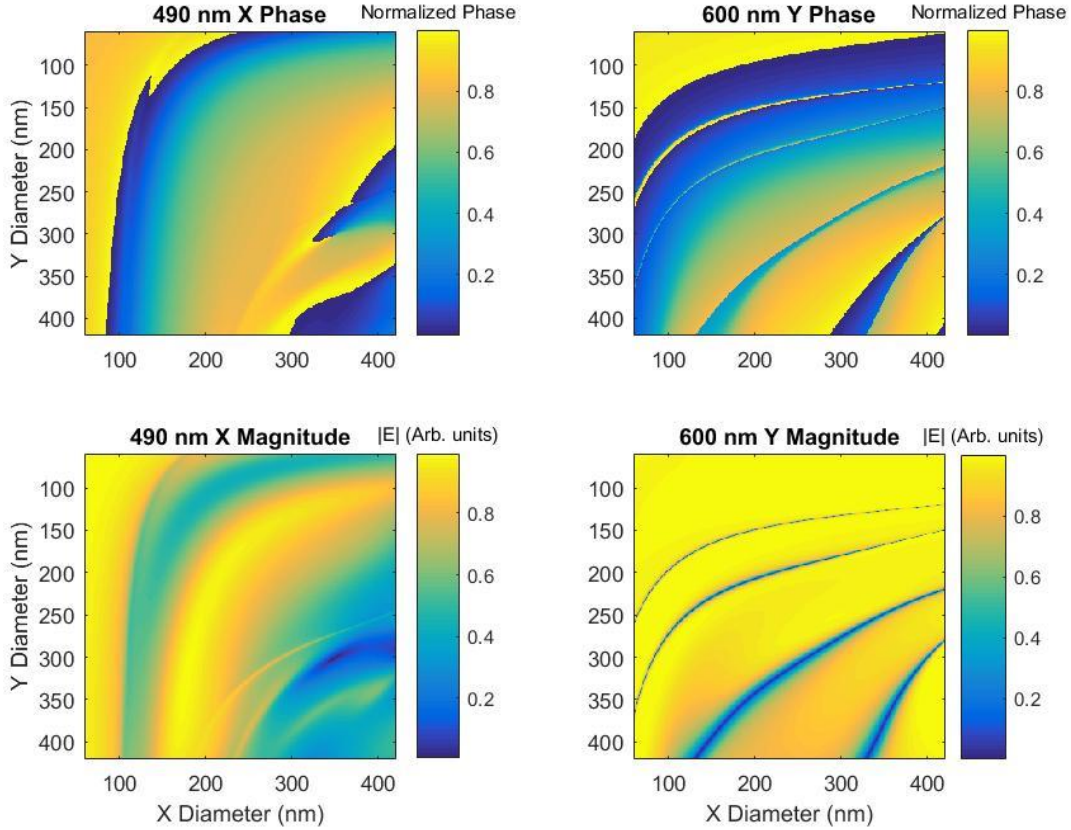


Figure 10: Transmission coefficients for the subwavelength elements that support wavelength multiplexing capability at 490 nm and 600 nm with polarization coding. Both the magnitude and phase on transmission are shown for x-polarized light at 490 nm and y-polarized light at 600 nm.

The determined subwavelength elements were then tested by generating different phase distributions for each input condition. In particular, the Gerchberg-Saxton algorithm was used to determine the phase necessary for making an H-shaped pattern and a V-shaped pattern. The metasurface was designed to make the H-shaped pattern under the 490 nm x-polarized

illumination condition, while a V-shaped pattern would be made under the 600 nm y-polarized condition. The metasurface was simulated in FDTD and the electric field measured near the metasurface was then Fourier transformed to produce the far-field diffraction pattern. **Figure 11** shows clearly that the patterns generated under the different illumination conditions are distinct, indicating that the subwavelength elements function as designed. Note that the intensity profiles shown are zoomed in on the hologram pattern itself and do not show the zero order diffraction spot. For visualization purposes this is simpler to see as the zero order diffraction spot was far more intense than the surrounding intensity patterns.

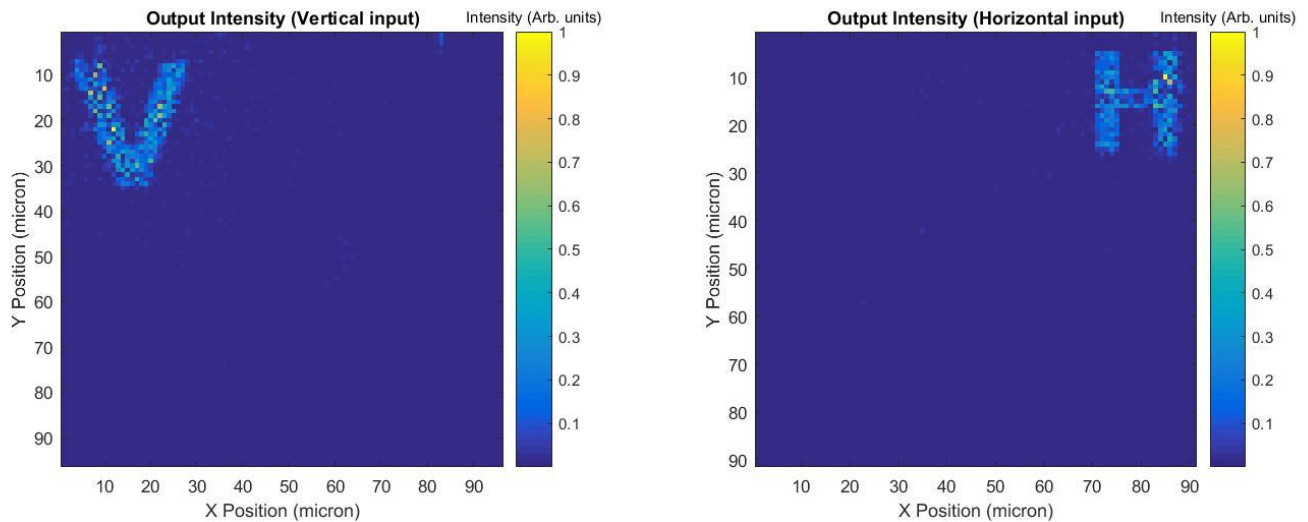


Figure 11: Output intensity profiles for y-polarized light at 600 nm and x-polarized light at 490 nm. Note that the units are arbitrary as this is in the far-field and that between the two plots the coordinate systems are not equivalent. The intensity profiles were generated by Fourier transforming the near-field electric field measured above the metasurface via FDTD simulation. Here the intensity profiles shown are zoomed in on the holograms themselves and do not show the zero order diffraction spot.

While this method appears to give good results, generating distinct intensity patterns for the two different input conditions, it is inherently limited because it is not truly multiwavelength as it relies on the input polarization as well. Since it is necessary to have an encoded polarization state along with the difference in wavelength, this technique is only applicable to a subset of the problems for which a truly multiwavelength device would work.

4.3 Exploiting Phase Shifts Greater Than 2π

The previous approaches to solving the multiwavelength operation problem required brute force parameter sweeps that would allow you to span arbitrary combinations of $(\Phi_{\lambda_1}, \Phi_{\lambda_2})$ pairs. While this technique can work, it is limited because it does not directly address the cause of chromatic aberrations in metasurfaces. In order to address these aberrations directly, it is necessary to take a step back to understand how they arise.

4.3.1 Chromatic Aberrations in Metasurfaces

If light of wavelength λ is normally incident on a dielectric slab of height L and refractive index n , then the phase shift θ accumulated upon transmission is given by (4):

$$(4) \theta = \frac{2\pi nL}{\lambda}$$

This phase shift is inversely proportional to the wavelength. In the case of a metasurface, a similar phase shift is experienced except that the refractive index parameter n is replaced with an effective refractive index n_{eff} which is a function of both the subwavelength geometry and its material properties³⁵. RCWA simulations verify this $1/\lambda$ dependence for the metasurface subwavelength elements and in particular, **Figure 12** depicts the transmission phase as a function of wavelength for a metasurface cylindrical post made of silicon nitride with thickness 633 nm, periodicity 443 nm, and diameter 111 nm. The RCWA-calculated transmission phase data is fitted to a function of the form $\frac{A}{\lambda} + B$, where the A parameter is related to n_{eff} and B is an arbitrary constant that can be regarded as a constant phase offset. The fit shows a close match to the simulated transmission phase. Similar relationships exist for other subwavelength geometries and wavelengths and it arises naturally because of equation (4).

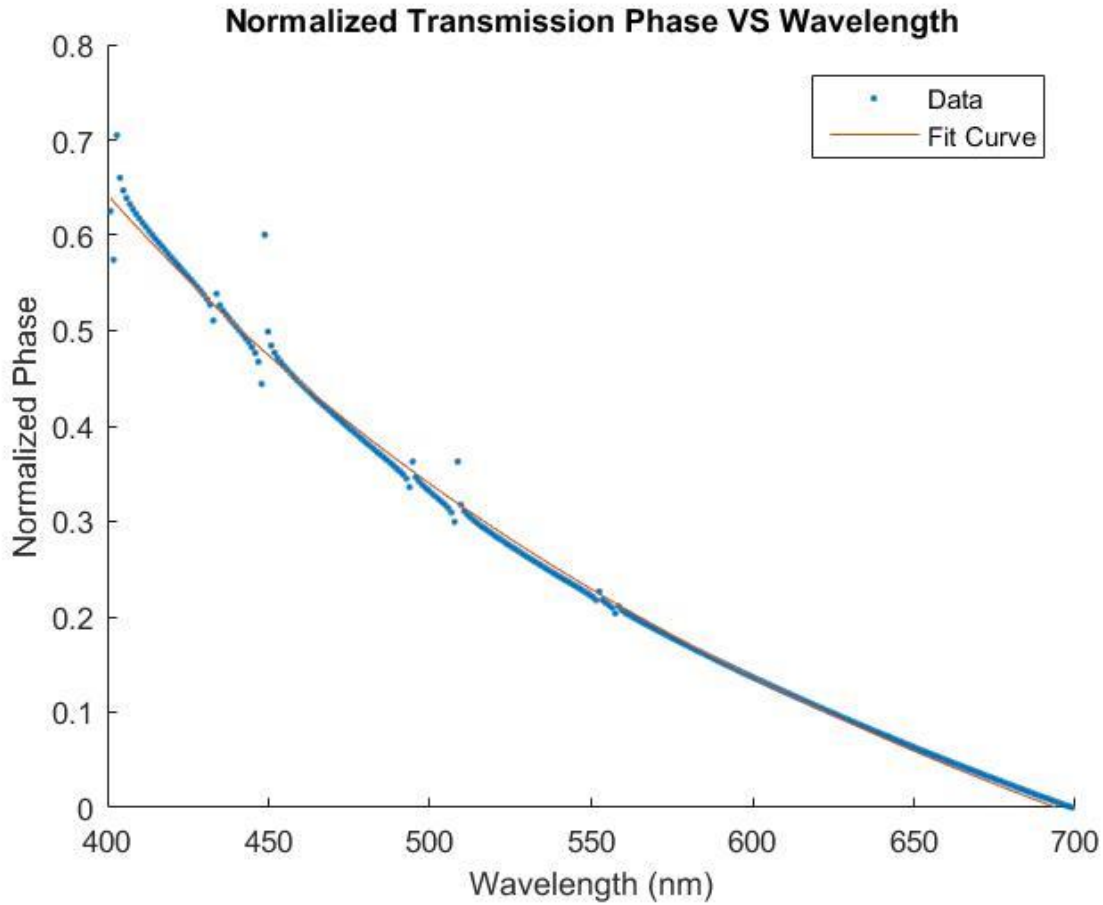


Figure 12: Plot of the transmission phase as a function of wavelength for a silicon nitride cylindrical post of thickness 633 nm, periodicity 443 nm, and diameter 111 nm. The transmission phase was calculated via RCWA. The data is fit to a function of the form $\frac{A}{\lambda} + B$ and the data shows very close agreement with this model.

In the case of a metasurface lens designed to operate at wavelength λ , the phase profile necessary for focusing at a focal length f is given by (5):

$$(5) \Phi(x, y) = \frac{2\pi}{\lambda} (\sqrt{(x)^2 + (y)^2 + f^2} - f)$$

From (5) we observe that the phase profile necessary for focusing is inversely proportional to λ , just as the individual subwavelength elements of a metasurface are inversely proportional to λ as in **Figure 12**. It would seem then that if you design a lens using (5) for a particular λ and then send in a wavelength different from the design wavelength, the metasurface

should still behave as a lens with focal length f ; both the subwavelength elements' phase shift and the overall phase profile would scale by the same amount, equal to the ratio of the design wavelength and the test wavelength. This statement is accurate, and in fact if you could actually implement (5), then the designed metasurface would have no chromatic aberrations; however, in practice chromatic aberrations do arise due to how (5) is implemented³⁵.

When subwavelength elements are designed, phase shifts from 0 to 2π are achievable by altering an element's geometry—in the case of our silicon nitride cylindrical posts, the duty cycle (i.e. *diameter/periodicity*) is swept from 0 to 1, causing the output phase to change from 0 to 2π . We know that these phase shifts are for a particular design wavelength, and from the $1/\lambda$ dependence of the phase, if we test the same pillar and duty cycle range the phase curve should change by a factor of $\frac{\lambda_1}{\lambda_2}$, where λ_1 is the original design wavelength and λ_2 is the new wavelength. This means that while for λ_1 the duty cycle sweep spans 0 to 2π , for λ_2 it spans 0 to $\frac{2\pi\lambda_1}{\lambda_2}$.

When a lens profile is implemented for the design wavelength λ_1 , going out from the origin the duty cycle of the pillars will increase as the phase increases from 0 to 2π . When the phase reaches 2π , due to the modular nature of phase, it will wrap back to 0 and correspondingly the duty cycle must wrap back as well such that the appropriate phase is implemented. In the case of λ_2 being passed through this lens, as you move out from the origin the correct phase will be achieved until you reach $\frac{2\pi\lambda_1}{\lambda_2}$. At this point, the phase wraps from 0 to 2π for λ_1 , but for λ_2 the wraparound in phase occurs at $\frac{2\pi\lambda_1}{\lambda_2}$ instead, creating a phase discontinuity for λ_2 . These discontinuities occur at every instance in which the phase for λ_1 wraps back to 0 and because of this, the phase profile implemented for λ_2 is not the lens phase profile, but some other profile

with quasiperiodic phase discontinuities. These phase-wrapping discontinuities are the cause of chromatic aberrations in metasurfaces³⁵.

4.3.2 Least Common Multiple Phase Approach

In understanding that phase-wrapping discontinuities are the cause of chromatic aberrations in metasurfaces, we devised a solution to eliminate these discontinuities and thereby eliminate chromatic aberrations. We know that for a metasurface designed for operation at λ_1 , there will be phase-wrapping points when the phase is 2π , and for another wavelength λ_2 there will be discontinuities at $\frac{2\pi\lambda_1}{\lambda_2}$. If the phase-wrapping points for λ_2 represented a change in phase from 0 to 2π , and not a discontinuity, then the metasurface could operate at both wavelengths without chromatic aberrations.

In the trivial case where $\lambda_1 = \lambda_2$, it is obvious that this condition is satisfied as $\frac{2\pi\lambda_1}{\lambda_2} = 2\pi$. Due to the modular nature of phase, this concept can be extended to cases where $\lambda_1 \neq \lambda_2$. In general, if we want the phase-wrapping points to only occur when the phase goes from 0 to 2π for both wavelengths, we can set the relation $\frac{2\pi\lambda_1 n}{\lambda_2} = 2\pi m$ where m and n are integers, yielding $n\lambda_1 = m\lambda_2$. This relation means that we need geometric parameters such that when the duty cycle is swept, phases from 0 to $2\pi n$ and 0 to $2\pi m$ are achieved for λ_1 and λ_2 respectively. Determining the values of m and n is equivalent to finding the least common multiple (LCM) of the two wavelengths. To understand this better, we can take an example in which $\lambda_2 = 2\lambda_1$. This gives $n = 2$ and $m = 1$, requiring that for λ_2 we achieve phase shifts from 0 to 2π and for λ_1 we span 0 to 4π . If we then design a lens for λ_1 , as we move out from the origin the phase and duty cycle increase. The same relationship of increasing duty cycle holds for λ_2 as well. At the point at which the phase becomes 2π for λ_1 , since $\lambda_2 = 2\lambda_1$, the phase is π for λ_2 . Before when we

reached 2π phase we would wrap around to 0 and would then wrap around in duty cycle as well; however, now with 0 to 4π phase achievable for λ_1 , the duty cycle does not have to wrap around until 4π phase is reached. When 4π phase is reached for λ_1 , this exactly coincides with when λ_2 reaches 2π phase. At this point, the phase wraps back to 0 for both λ_1 and λ_2 without any discontinuity.

To test the validity of this method, it was applied to the case where a lens was designed to operate with the same focal length for both 400 nm and 800 nm light. To do this 0 to 4π phase was necessary for 400 nm and 0 to 2π phase was necessary for 800 nm. For silicon nitride cylindrical posts with a thickness of 1100 nm and periodicity of 200 nm the amplitude and phase transmission characteristics are shown in **Figure 13** for both 400 nm and 800 nm input light. Using the duty cycle parameters from **Figure 13** a lens was designed for 400 nm operation using the full 0 to 4π range of phases. The lens was designed to operate at a focal length of 20 microns and **Figure 14** shows the focal spots for both 800 nm and 400 nm sources. The lens was simulated via FDTD and the focal spots occur at the designed focal length for both frequencies, indicating that the lens does not suffer from chromatic aberrations at 400 nm and 800 nm.

The concept of finding the LCM of the two design wavelengths and then exploiting phase shifts which go beyond 0 to 2π can be generalized. For the case of more than two wavelengths, the LCM of all the wavelengths of interest must be determined. It is crucial that when the parameters are found which give the necessary phase shifts, that the curves are smooth and uniform amplitude is maintained. In cases where there are resonances in the phase curve, the $1/\lambda$ relationship for phase does not hold which then prevents the LCM method from working. To ensure there are no resonances it has been found that high aspect ratio structures tend to perform better, generating smoother phase curves with uniform amplitude. The need for high aspect ratio

structures imposes a serious limitation to this method in terms of fabrication. Additionally, since this method only works for wavelengths for which the $1/\lambda$ phase relationship holds, it can only be used in instances in which dispersion is negligible across the design wavelengths.

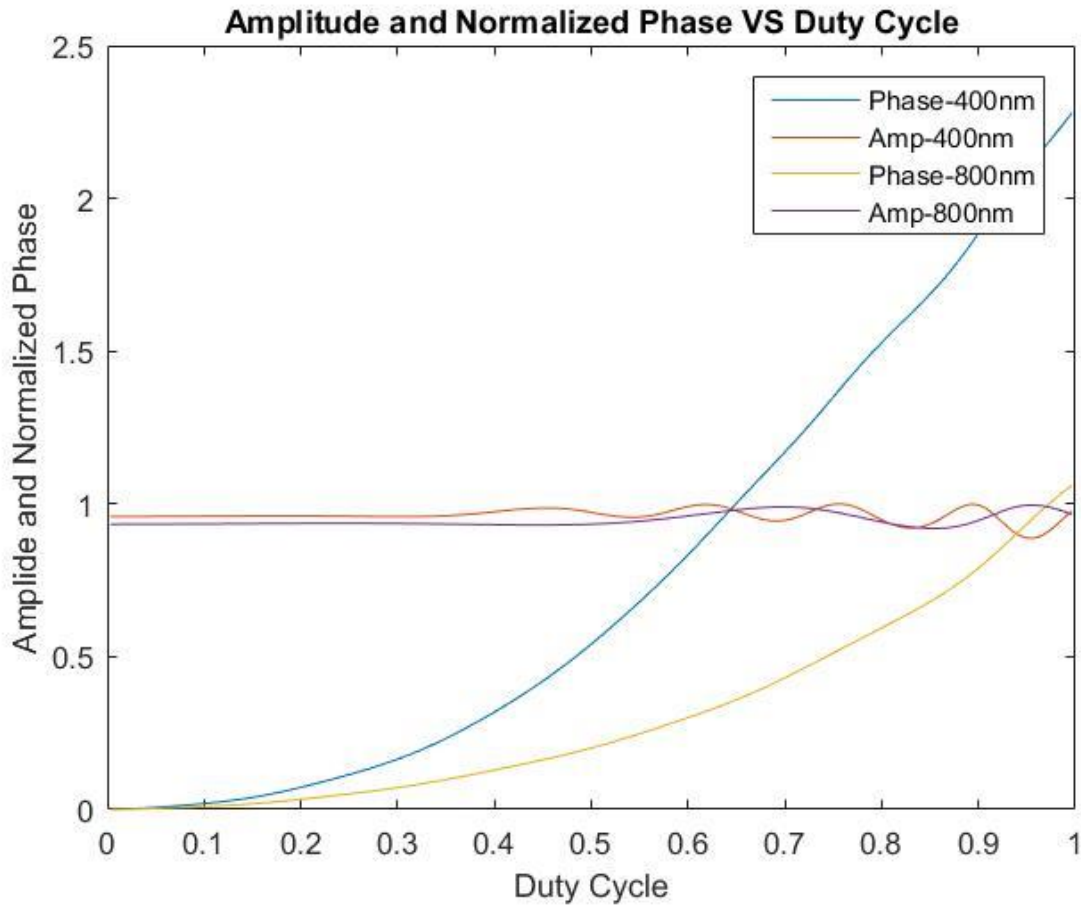


Figure 13: RCWA-calculated transmission amplitude and phase as a function of duty cycle for both 400 nm and 800 nm inputs.

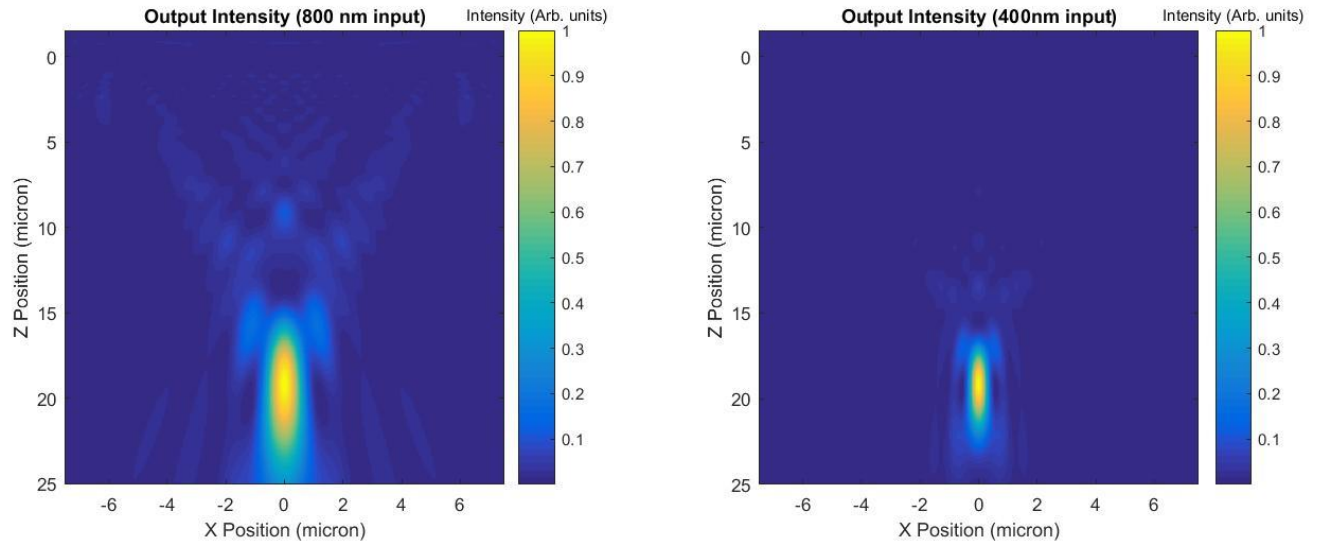


Figure 14: FDTD-simulated focal spots for the lens designed for operation at 400 nm and 800 nm without aberrations. The intensity profiles are in the $y = 0$ plane and show the focal spots along the propagation axis (i.e. the z -axis). Both focal spots occur near the designed focal plane at 20 microns. The 800 nm focal spot is larger as expected because of the difference in wavelength.

Chapter 5: Tunable Asymmetric Elements for Reconfigurable Metasurfaces

One of the limitations of current metasurfaces is that they are static structures only capable of performing a single operation, or perhaps two to three operations at most if the structure has multiplexing capability. In digital electronics, field-programmable gate arrays (FPGAs) are versatile integrated circuits capable of performing a wide variety of functions depending on how it is programmed. In optics, the closest analogue is likely a spatial light modulator (SLM), which modulates spatial light distributions in either phase, amplitude, or both. SLMs are versatile components, but are limited in terms of pixel size, which is on the order of $2 \mu\text{m} \times 2 \mu\text{m}$. Such large pixel size is unsuitable for nanoscale photonics applications in which subwavelength resolution is necessary, as in the case of a metasurface. To achieve a device suitable for such applications, a tunable and compact phase shifter is necessary. Ideally, large phase shifts should be achievable with only small external perturbations. With very small changes, resonator-based phase shifters can produce very large changes in phase; however, these changes in phase also go hand-in-hand with large fluctuations in amplitude. For many applications, such large changes in amplitude cannot be tolerated. Here, a methodology is presented for a compact phase shifter which can achieve large changes in phase with negligible change in amplitude. This phase shifting device is first explored from a very abstract model, is then simulated as a standalone device, and is ultimately tested acting in an ensemble manner as part of a metasurface.

5.1 Asymmetric Fabry-Perot Tunable Phase Concept

5.1.1 Ideal Model

An asymmetric Fabry-Perot cavity is a device which is capable of providing a large change in phase with minimal to no change in amplitude. Such a cavity consists of two parallel reflectors with different values of reflectivity, as shown in **Figure 15**. If we model the bottom reflector as being a perfect mirror and assume the cavity itself is lossless, then for all input frequencies the output amplitude will be unity. This is intuitive because with a perfect mirror, all the light that enters the cavity must eventually leave. More rigorously, we can show this by superposing the initial reflected beam with all of the subsequent beams which pass out of the cavity. If the input wave has amplitude A , the top mirror has external reflectivity r , internal reflectivity r' , ingoing transmission amplitude t , outgoing transmission amplitude t' , and the phase accumulated in one round trip in the cavity is δ , then the initial reflected beam is given by:

$$(6) E_{r1} = Ar$$

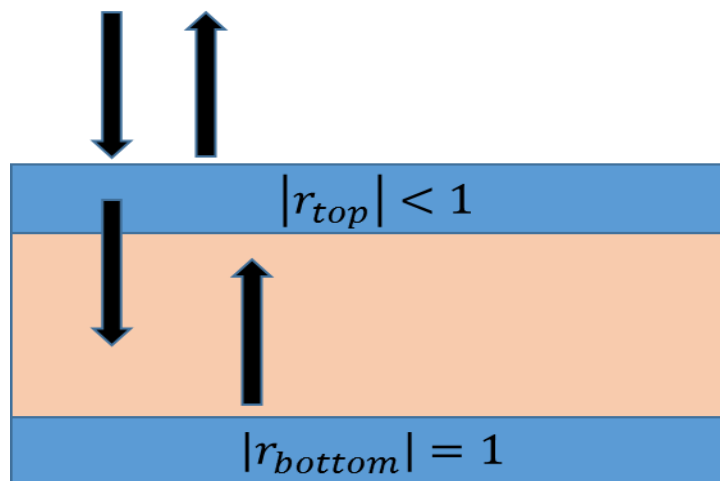


Figure 15: Schematic representation of an asymmetric Fabry-Perot cavity in which the reflectivities of the two mirrors are unequal. Here the special case where the bottom mirror is a perfect reflector is represented.

The second outgoing beam passes through the top mirror, picks up a δ phase shift in the cavity, and then passes back out the top mirror, so it is given by:

$$(7) E_{t1} = Att'e^{i\delta}$$

The third outgoing beam is similar to the second except rather than transmitting through the top after one trip, it takes an additional trip, picking up another δ phase, and scaling by a factor of r' :

$$(8) E_{t2} = Att'r'e^{2i\delta}$$

Extending this to an infinite number of outgoing beams, the total E-field outside the cavity can be expressed as below:

$$(9) E_{total} = Ar + Att'e^{i\delta} \sum_{n=0}^{\infty} (r'e^{i\delta})^n$$

Since $|r'| < 1$, the infinite series converges, and utilizing $tt' - rr' = 1$ and $r = -r'$ by energy conservation, the expression simplifies to:

$$(10) E_{total} = \frac{A(r+e^{i\delta})}{1+re^{i\delta}}$$

From (10), we see that regardless of the value of r , $|E_{total}| = 1$. Unlike the amplitude, the phase is highly dependent on the value of r . To understand the relationship between r and the phase of E_{total} , the output phase θ is plotted against the cavity phase δ for different values of r in **Figure 16**. Physically, these plots show the effect of changing either the operating wavelength λ , the refractive index of the cavity n , or the length of the cavity L , as the cavity phase $\delta = \frac{2\pi nL}{\lambda} + \phi_0$, where ϕ_0 is a constant phase offset due to reflection off the bottom mirror. From this ideal model, we see that there is a regime in which the phase changes very rapidly, exhibiting asymptotic-like behavior near $\delta = 0$. We can also see that for higher values of r , this change in phase is much more rapid near $\delta = 0$. In terms of designing a compact phase shifter, this rapid phase change near $\delta = 0$ for high values of r can be exploited.

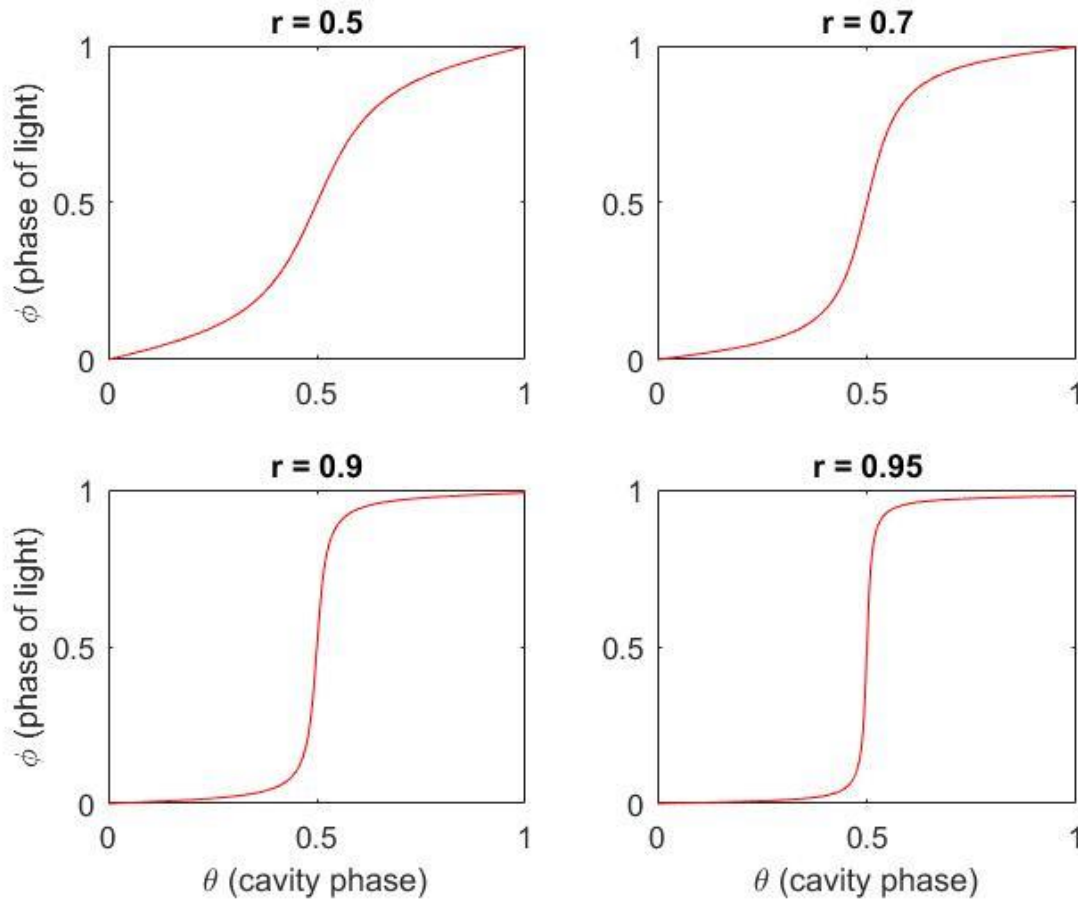


Figure 16: Plots of the normalized phase of the output light from cavity versus the normalized phase of the cavity itself for different reflectivity values for the top mirror. For higher values of r the phase curve exhibits a faster transition.

5.1.2 Simulated Full Cavity

To verify the phase-shifting behavior of the abstract model for the asymmetric Fabry-Perot cavity, a structure consisting of a high reflectivity grating on top of slab of dielectric, on top of a perfect electrical conductor (PEC) was simulated. The grating was of height 360 nm, periodicity 800 nm, and width 440 nm. The dielectric slab, which constitutes the cavity itself, was of thickness 710 nm. Both the cavity and the grating were made of silicon and the input was 1550 nm and was polarized perpendicular to the grating lines. In FDTD simulation, the refractive

index of the cavity was swept to model changing the cavity phase. The corresponding phase and amplitude of the wave reflected off of the cavity are given in **Figure 17**. We see that this cavity exhibits similar asymptotic-like behavior with the phase spiking suddenly while the amplitude remains uniform, confirming the accuracy of the abstract model for the asymmetric Fabry-Perot cavity.

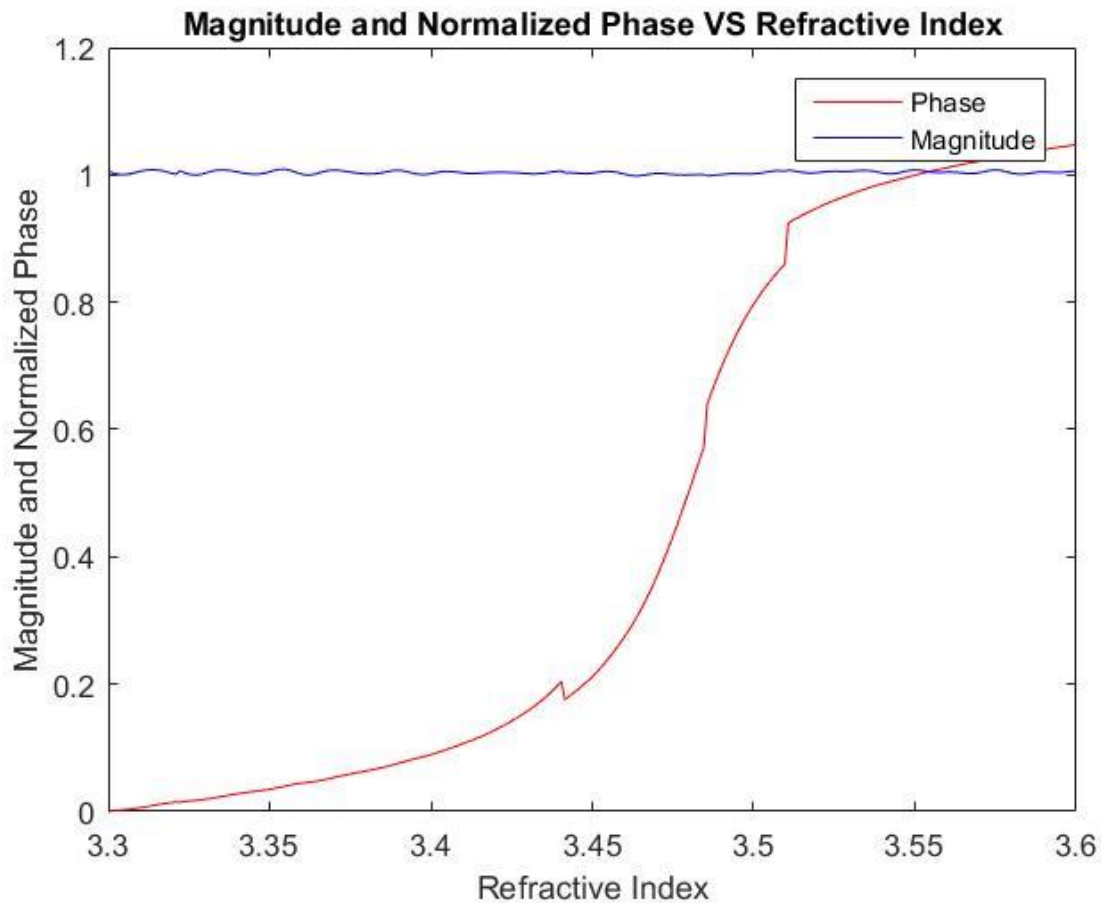


Figure 17: The magnitude and reflection phase shown as a function of the cavity refractive index for the FDTD-simulated asymmetric Fabry-Perot cavity. The top mirror is modelled using a high reflectivity grating, while the bottom mirror consists of a layer of perfect electrical conductor (PEC). The magnitude remains uniform at 1 for whole sweep range of the refractive index.

5.2 Single Element Asymmetric Phase Shifters

While the simulated cavity exhibits the desired behavior of large phase change with negligible change in amplitude, the cavity itself is modelled with periodic boundary conditions that extend to infinity. In practice, this type of cavity could have finite extent and likely still support similar behavior; however, to have the compact and high resolution capability as originally specified, we will need a phase-shifting device with subwavelength spatial extent that can be patterned across a metasurface to implement dynamic and arbitrary spatial phase profiles. While the previously simulated cavity has an infinite number of grating lines, it is intuitive to imagine decreasing the spatial extent to a finite number of lines and still achieving similar performance as long as the structure is still large. As you decrease the number of lines even further, we'd expect the behavior to further deviate from that of the original cavity, but still possibly maintain some similar qualitative behavior. In the limit that the number of grating lines goes to 1, then all you have left of your "cavity" is a single grating line on top of the perfect mirror; however, it is important to understand that if we have a metasurface, that many of these "cavities" will be patterned across the structure in a periodic manner. The periodic nature of these "cavities" constitutes a grating which rests on top of the perfect mirror.

To assess this device, RCWA was used to calculate the phase and amplitude on reflection from such a structure. The device was modelled by a 500 nm thick layer of gold with refractive index $n = 0.583$ and $k = 9.864$, beneath a silicon grating of height 658 nm, periodicity 800 nm, and width 620 nm. The results of this simulation are shown in **Figure 18** where we see similar behavior with large phase change, except that here the amplitude dips substantially when the phase changes also. This change in amplitude can be attributed to the change in substrate

material from the lossless PEC to the lossy gold substrate, rather than the failure of the methodology.

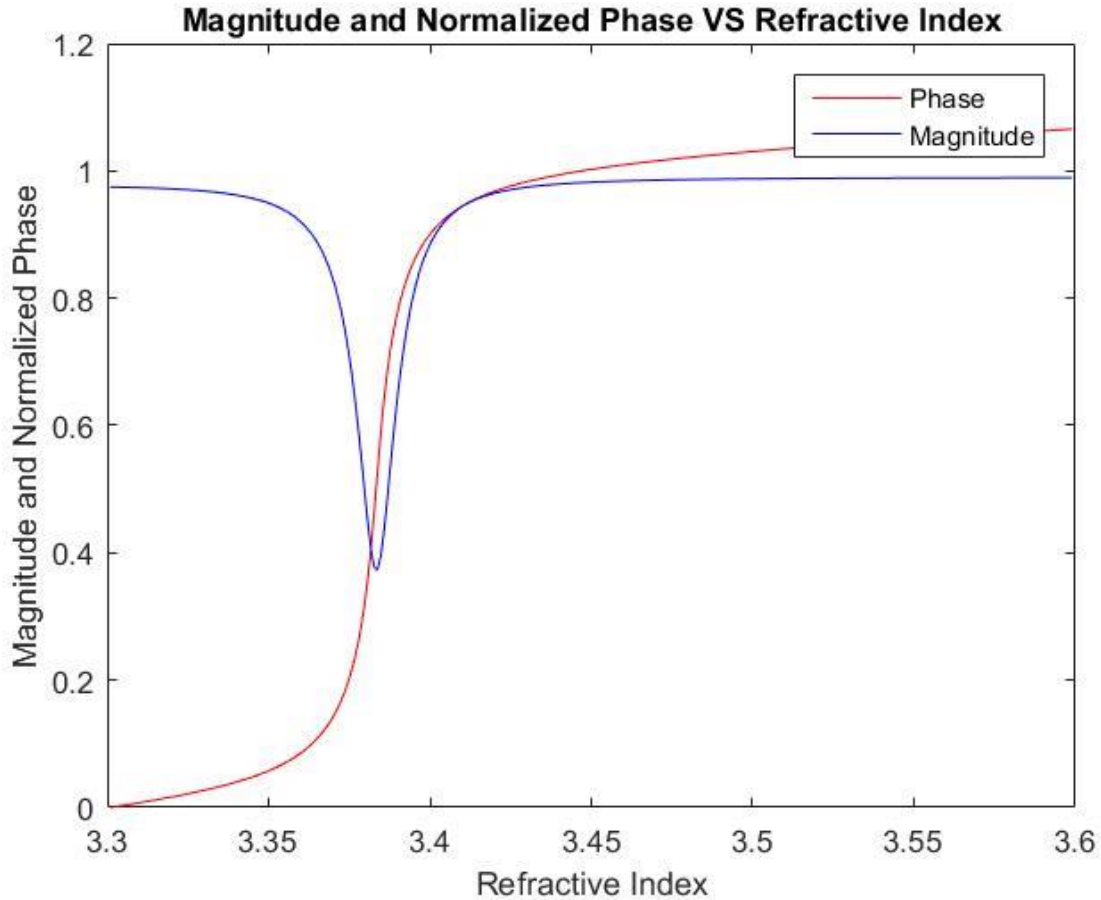


Figure 18: The magnitude and reflection phase shown as a function of the grating refractive index for the RCWA-simulated single grating line “cavities” with a gold-based bottom mirror. The bottom perfect mirror is modelled using a 500 nm layer of gold. The magnitude dips substantially near the phase jump, indicating loss in the gold layer.

To achieve a practical device with minimal loss, a dielectric mirror consisting of a distributed Bragg reflector (DBR) was placed beneath the silicon grating in place of the previous gold layer. The DBR consisted of four layers of pairs of silicon and silicon dioxide with thicknesses optimized for operation at 1550 nm. After some optimization of the height of the grating lines, the reflection phase and amplitude of this DBR-based device were determined and

are shown in **Figure 19** The grating was of height 516 nm, periodicity 800 nm, and width 620 nm. We see that now with a dielectric mirror modelling the perfect bottom mirror, that the single grating line “cavities” still produce asymptotic-like phase curves, similar to that of the original asymmetric Fabry-Perot cavity.

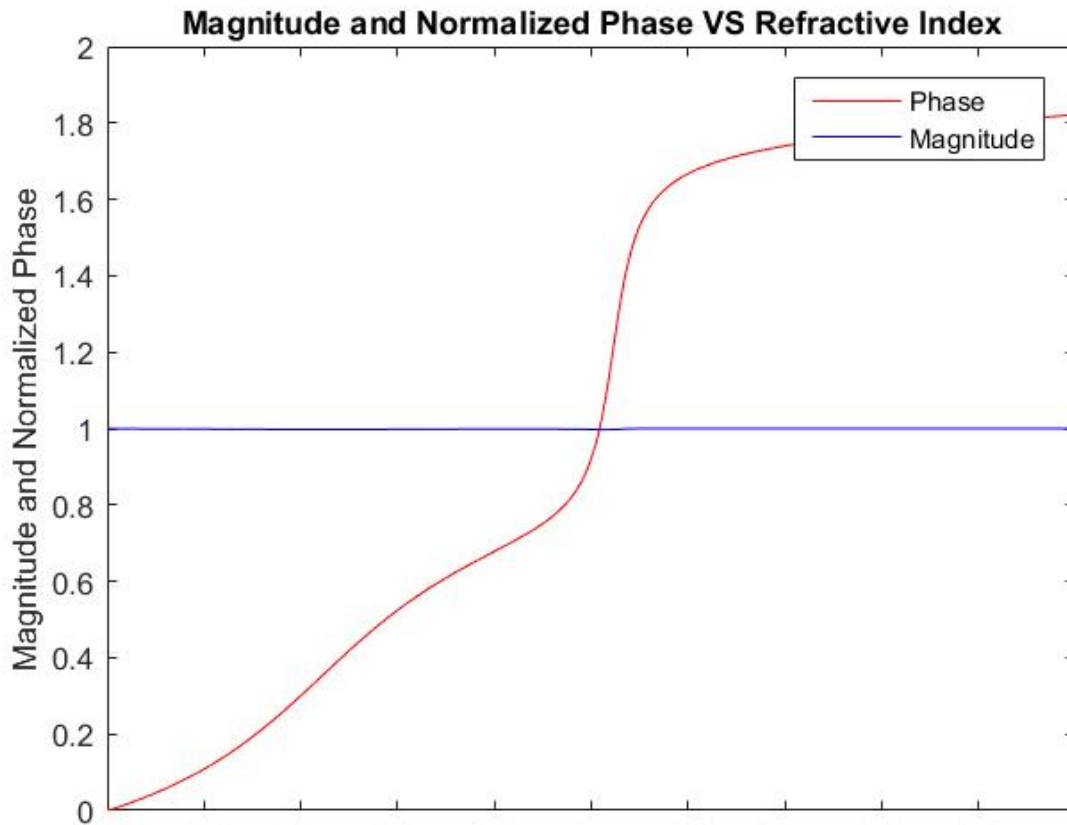


Figure 19: The magnitude and reflection phase shown as a function of the grating refractive index for the RCWA-simulated single rectangular grating line “cavities” with a DBR-based bottom mirror. The magnitude remains at unity for the whole sweep range of refractive index.

Up until this point, the simulations for the asymmetric cavity structures have only used rectangular grating lines. Phase shifters made of such grating lines would only be capable of implementing 1-D phase profiles, such as that for a cylindrical lens. To assess whether such a device would work for 2-D phase profiles, the rectangular lines were replaced with cylindrical posts, also made of silicon. The posts were of height 596 nm, periodicity 800 nm, and diameter

680 nm. The phase and amplitude on reflection from the structure are shown in **Figure 20**. We see that even for cylindrical posts, the rapid change in phase similar to that of an asymmetric Fabry-Perot cavity is still possible.

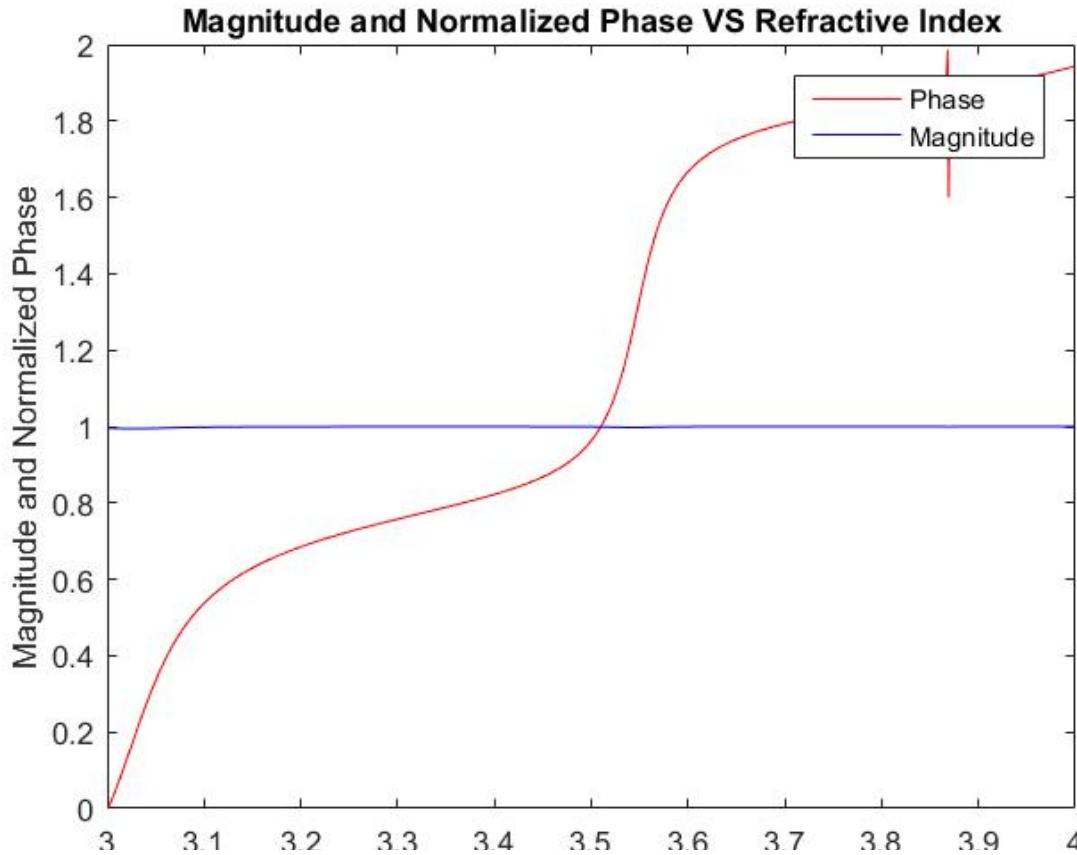


Figure 20: The magnitude and reflection phase shown as a function of the grating refractive index for the RCWA-simulated single cylindrical post “cavities” with a DBR-based bottom mirror. The magnitude remains at unity for the whole sweep range of refractive index.

5.3 Simulation Testing Results

To assess the phase shifting behavior of the subwavelength elements, different phase profiles were tested for both the 1D and 2D elements. In particular, two different devices were designed, one which can implement only 1D phase profiles and another for imparting 2D phase profiles. These two devices are static in terms of geometry and structure, but by individually

altering the refractive indices of the grating lines in each, they provide the ability to implement arbitrary phase profiles. At this stage the mechanism for changing the refractive index is not fully developed, but there are several options including thermal tuning, complex oxides, phase change materials, and free carrier effects. With all of these refractive index modulation techniques, the modulation range is very small (e.g. for thermal tuning the temperature coefficient for refractive index is $1.86 * 10^{-4} K^{-1}$); however, by exploiting the rapid phase change regime of our asymmetric subwavelength elements, we do not need a large change in refractive index in order to achieve a 0 to 2π phase modulation range.

5.3.1 1D Phase Profile Device

To assess the 1D phase elements a structure was designed of consisting of a total of 112 grating elements occupying a width of 90 microns patterned across a high reflectivity DBR. Using the calculated phase characteristics of the 1D elements in **Figure 19**, the necessary phase profiles were determined for cylindrical lenses with focal lengths of 150 and 250 microns, based on the cylindrical lens phase profile equation below:

$$\Phi(x) = \frac{2\pi}{\lambda} (\sqrt{x^2 + f^2} - f)$$

The refractive indices corresponding to these phase points were mapped to the elements across the structure to implement the phase profile. The structures were then simulated in FDTD and the results are presented in **Figure 21** and **Figure 22** for the 150 and 250 micron focal lengths respectively. The results indicate that the 1D phase profile device was successful at implementing the profile of a cylindrical lens and that it supports the capability of implementing different profiles based on the same structure. The focuses generated from each cylindrical lens designed are near the design 150 and 250 microns; however, they are shifted slightly and there

are additional bright spots corresponding to inefficient focusing. In the focal planes themselves, a clean and nice high intensity focal line is observed for both designs.

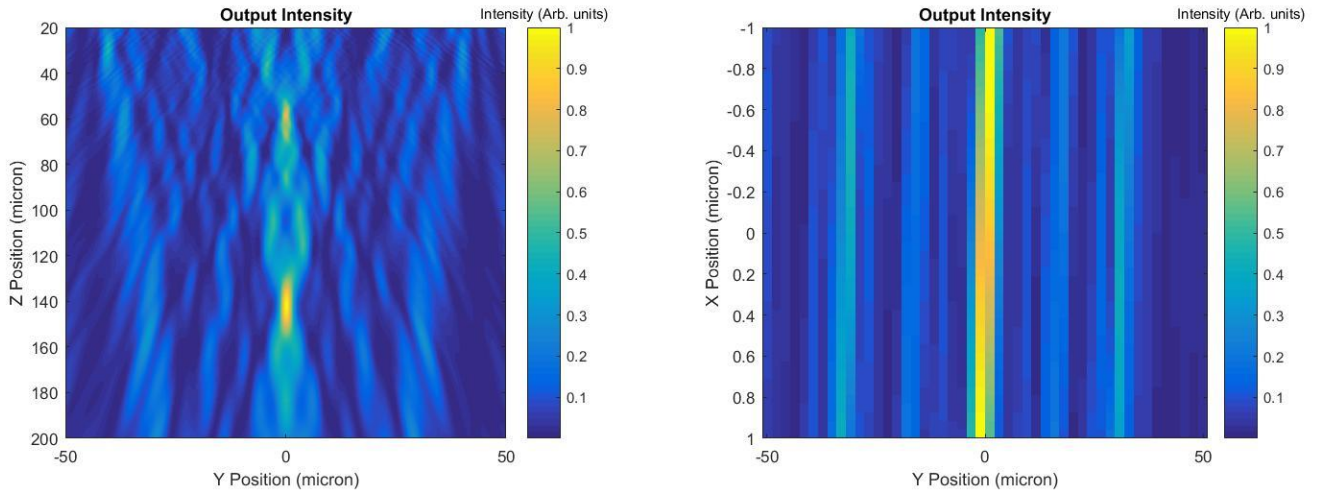


Figure 21: Intensity profiles for the cylindrical lens designed for a focal length of 150 microns. On the left the focal spot is shown in the $x = 0$ plane, showing the focal spot along the propagation direction. On the right the profile in the focal plane is shown, indicating a clear line focus as expected for a cylindrical lens.

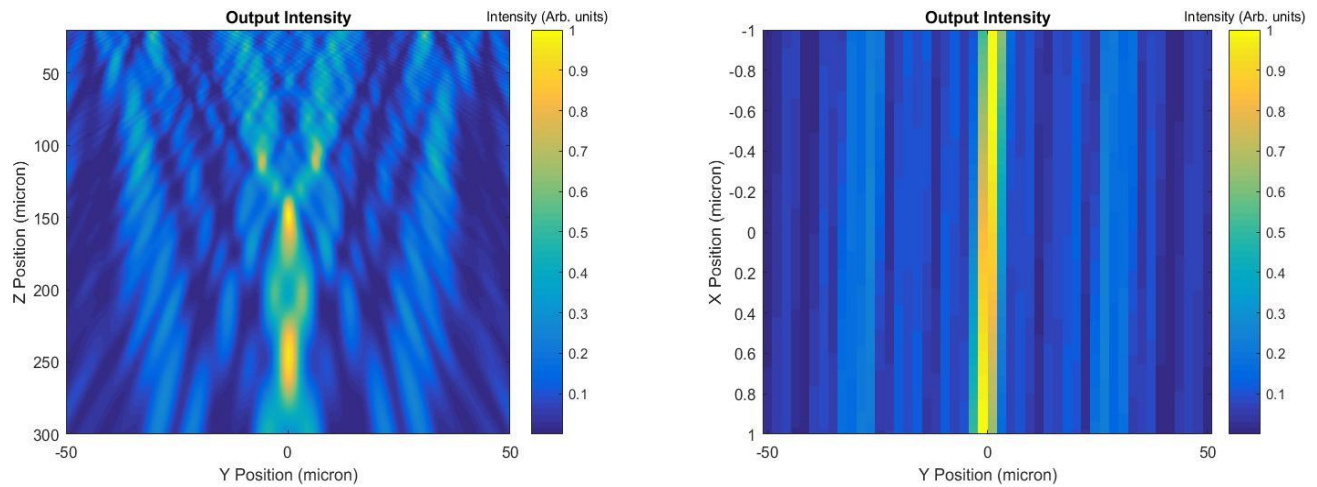


Figure 22: Intensity profiles for the cylindrical lens designed for a focal length of 250 microns. On the left the focal spot is shown in the $x = 0$ plane, showing the focal spot along the propagation direction. On the right the profile in the focal plane is shown, indicating a clear line focus as expected for a cylindrical lens.

5.3.2 2D Phase Profile Device

For the 2D phase elements, a device with a radius of 20 microns was designed using 1941 cylindrical post elements from **Figure 20** on top of a DBR. To assess the device, phase profiles were implemented for lenses of two different focal lengths. By testing lenses of different focal lengths, the capability of dynamically implementing different profiles can be evaluated. **Figure 23** presents the FDTD simulation results for lenses with focal lengths of 30 and 50 microns. The intensity profiles for the lenses indicate successful focusing, although in the case of the 50 micron profile, the focus is less intense and there appears to be inefficient funneling of light into other bright spots. In the case of the 30 micron profile, the focus is very prominent; however, both the 30 and 50 micron focal spots are shifted off slightly from their designed focal planes.

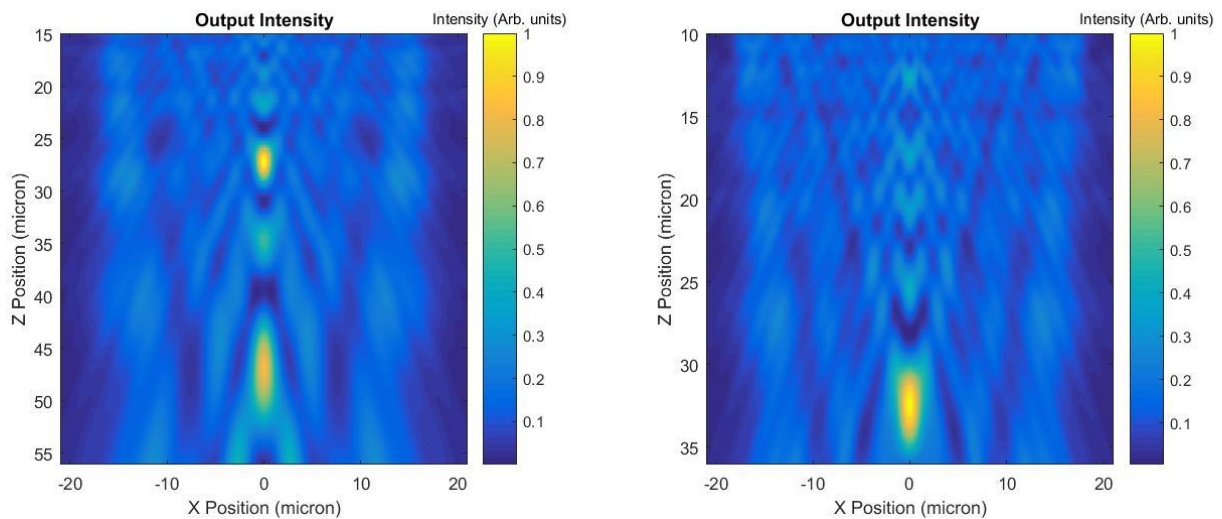


Figure 23: Intensity profiles for the lenses designed for focal lengths of 50 microns (left) and 30 microns (right).

Chapter 6: Conclusion and Outlook

This thesis details simulations and theoretical work for designing dielectric metasurface subwavelength scattering elements. The designed scattering elements are optimized for different functionalities and represent an effort toward achieving compact optical sensors. In particular, designs were presented for silicon nitride based scattering elements for polarization-multiplexed metasurfaces in the visible regime, frequency-multiplexed metasurfaces and a general methodology for eliminating chromatic aberrations at discrete wavelengths, and silicon-based tunable and compact phase-shifting elements for implementing reconfigurable phase profiles.

For the polarization-multiplexed scattering elements in the visible regime, rigorous coupled-wave analysis (RCWA) simulations were used to determine transmission coefficients for various geometries. Using the RCWA-calculated transmission characteristics, metasurfaces were designed for implementing polarization-multiplexed holograms and focusing. These metasurfaces were tested via finite-difference time-domain (FDTD) simulations and results indicate successful multiplexing capability. In the future, these designs can be improved by overcoming the efficiency and crosstalk limitations by optimizing the parameters determined by RCWA.

Three different approaches to achieving multiwavelength operation were explored: dispersive phase engineering, encoding each wavelength with a distinct polarization state, and eliminating phase wrapping discontinuities by exploiting phase shifts greater than 2π . The dispersive phase engineering approach was deemed too challenging and inefficient in the visible regime as the wavelength difference was too small to achieve parameters which would allow spanning of all combinations of $(\Phi_{\lambda_1}, \Phi_{\lambda_2})$ pairs. The polarization coding method worked well in producing distinct holograms for different wavelengths, but in the long term this approach should

be modified as it does not represent a true frequency-multiplexed device as orthogonal polarizations are necessary for multiplexing capability. The third approach of exploiting phases greater than 2π worked well, achieving focusing in the same plane for both 400 nm and 800 nm inputs. This third approach is generalizable to other wavelength regimes, but requires that the $1/\lambda$ dependence of the output phase holds. As far as future experimental work goes, parameters for multiwavelength operation in a dispersionless regime which supports large phase shifts with low aspect ratios needs to be tested.

A design approach for making compact and tunable phase shifters for metasurfaces was presented. Compared to some methodologies in which amplitude changes hand-in-hand with phase and which require a large refractive index modulation range, the method presented in this thesis overcomes both of these limitations. Moving forward, parameters for these subwavelength phase shifters must be optimized so that phase profiles can be implemented more accurately. In terms of experiment, a next step forward would be making one of these tunable metasurfaces and first seeing if the RCWA-simulated phase curve can be reproduced by interferometric measurements.

Altogether, this thesis helps advance the state of art devices in the field of dielectric metasurface optics. These improvements will help to achieve the goal of realizing a compact and efficient optical sensor. Integrating these components with other technologies could help support infrastructure for the Internet of Things (IoT) and implantable nanoscale sensors.

References

- [1] Pendry, J. B. Negative refraction makes a perfect lens. *Phys. Rev. Lett.* 85, 3966–3969(2000).
- [2] Shelby, R. A., Smith, D. R. & Schultz, S. Experimental verification of a negative index of refraction. *Science* 292, 77–79 (2001).
- [3] Yao, J. et al. Optical negative refraction in bulk metamaterials of nanowires. *Science* 321,930 (2008).
- [4] Shalaev, V. M. Optical negative-index metamaterials. *Nature Photon.* 1, 41–48 (2007).
- [5] Poddubny, A., Iorsh, I., Belov, P. & Kivshar, Y. Hyperbolic metamaterials. *Nature Photon.* 7,948–957 (2013).
- [6] Yu, N. et al. Light Propagation with Phase Discontinuities: Generalized Laws of Reflection and Refraction. *Science* 334, 333-337, doi:10.1126/science.1210713 (2011).
- [7] Lin, D.; Fan, P.; Hasman, E.; Brongersma, M. L., Dielectric Gradient Metasurface Optical Elements. *Science* 2014, 345, 298-302.
- [8] Kildishev, A. V., Boltasseva, A. & Shalaev, V. M. Planar Photonics with Metasurfaces. *Science* 339, doi:10.1126/science.1232009 (2013).
- [9] Yu, N. & Capasso, F. Flat optics with designer metasurfaces. *Nat Mater* 13, 139-150, doi:10.1038/nmat3839 (2014).
- [10] Aieta, F. et al. Aberration-Free Ultrathin Flat Lenses and Axicons at Telecom Wavelengths Based on Plasmonic Metasurfaces. *Nano Letters* 12, 4932-4936, doi:10.1021/nl302516v (2012).
- [11] Arbabi, A., Horie, Y., Bagheri, M. & Faraon, A. Dielectric metasurfaces for complete control of phase and polarization with subwavelength spatial resolution and high transmission. *Nat Nano advance online publication*, doi:10.1038/nnano.2015.186
- [12] Saleh, Bahaa E. A., and Malvin Carl. Teich. "Fourier Optics." *Fundamentals of Photonics*. New York: Wiley, 1991. 108-56. Print.
- [13] C. E. Shannon, "Communication in the presence of noise", *Proc. Institute of Radio Engineers*, vol. 37, no.1, pp. 10–21, Jan. 1949.
- [14] Stork, W.; Streibl, N.; Haidner, H.; Kipfer, P., Artificial Distributed-Index Media Fabricated by Zero-Order Gratings. *Opt. Lett.* 1991, 16, 1921-1923.
- [15] Pancharatnam, S. Generalized theory of interference, and its applications. Part I. Coherent pencils. *Proc. Indian Acad. Sci. Sect. A* 44, 247–262 (1956).
- [16] Berry, M. V. Quantal phase factors accompanying adiabatic changes. *Proc. R. Soc. London A* 392, 45–57 (1984).
- [17] Arbabi, A., Horie, Y., Ball, A. J., Bagheri, M. & Faraon, A. Subwavelength-thick lenses with high numerical apertures and large efficiency based on high-contrast transmitarrays. *Nat Commun* 6, doi:10.1038/ncomms8069 (2015).
- [18] Fattal, David, et al. "Flat dielectric grating reflectors with focusing abilities." *Nature Photonics* 4.7 (2010): 466-470.
- [19] Aieta, F. et al. Aberration-Free Ultrathin Flat Lenses and Axicons at Telecom Wavelengths Based on Plasmonic Metasurfaces. *Nano Letters* 12, 4932-4936, doi:10.1021/nl302516v (2012).
- [20] Yu, N. et al. A broadband, background-free quarter-wave plate based on plasmonic metasurfaces. *Nano Lett.* 12, 6328–6333 (2012).

- [21] Ni, X., Ishii, S., Kildishev, A. V. & Shalaev, V. M. Ultra-thin, planar, Babinet-inverted plasmonic metalenses. *Light: Sci. Appl.* 2, e27 (2013)
- [22] Memarzadeh, B. & Mosallaei, H. Array of planar plasmonic scatterers functioning as light concentrator. *Opt. Lett.* 36, 2569–2571 (2011)
- [23] Pors, A., Nielsen, M. G., Eriksen, R. L. & Bozhevolnyi, S. I. Broadband focusing flat mirrors based on plasmonic gradient metasurfaces. *Nano Lett.* 13, 829–834 (2013)
- [24] Genevet, P. et al. Ultra-thin plasmonic optical vortex plate based on phase discontinuities. *Appl. Phys. Lett.* 100, 013101 (2012).
- [25] Pors, O. Albrektsen, I. P. Radko, S. I. Bozhevolnyi, *Sci. Rep.* 3, 2155 (2013).
- [26] S. Sun et al., *Nano Lett.* 12, 6223–6229 (2012).
- [27] Zhan, A. et al. Low-Contrast Dielectric Metasurface Optics. *ACS Photonics* 3, 209-214, doi:10.1021/acsp Photonics.5b00660 (2016).
- [28] Astilean, S., Lalanne, P., Chavel, P., Cambriil, E. & Launois, H. High-efficiency subwavelength diffractive element patterned in a high-refractive-index material for 633??nm. *Opt. Lett.* 23, 552-554, doi:10.1364/OL.23.000552 (1998).
- [29] Silva*, F. Monticone*, G. Castaldi, V. Galdi, A. Alù, and N. Engheta, “Performing Mathematical Operations with Metamaterials,” *Science*, Vol. 343. No. 6167, pp. 160-163, January 10, 2014.
- [30] Pors, Anders, Michael G. Nielsen, and Sergey I. Bozhevolnyi. "Analog computing using reflective plasmonic metasurfaces." *Nano letters* 15.1 (2014): 791-797.
- [31] Ni, Xingjie, et al. "An ultrathin invisibility skin cloak for visible light." *Science*349.6254 (2015): 1310-1314.
- [32] Yin, Xiaobo, et al. "Photonic spin Hall effect at metasurfaces." *Science*339.6126 (2013): 1405-1407.
- [33] Wang, Qian, et al. "Optically reconfigurable metasurfaces and photonic devices based on phase change materials." *Nature Photonics* 10.1 (2016): 60-65.
- [34] Aieta, Francesco, et al. "Multiwavelength achromatic metasurfaces by dispersive phase compensation." *Science* 347.6228 (2015): 1342-1345.
- [35] Arbabi, Ehsan, et al. "Multiwavelength polarization insensitive lenses based on dielectric metasurfaces with meta-molecules." arXiv preprint arXiv:1601.05847 (2016).
- [36] Wen, Dandan, et al. "Helicity multiplexed broadband metasurface holograms." *Nature communications* 6 (2015).
- [37] Gerchberg, R. W. & Saxton, W. O. A Practical Algorithm for the determination of phase from image and diffraction plane pictures. *OPTIK* 35, 237–246 (1971).